

Development of Ce/Cu co-doped dendritic mesoporous silica nanoparticles (DMSNs) as novel abrasive systems toward high-performance chemical mechanical polishing

Wenjin Zhou^a, Yang Chen^{a,*}, Chao Wang^{b,**}, Menghan Wang^a, Ailian Chen^{c,***}

^a School of Materials Science and Engineering, Changzhou University, Changzhou, Jiangsu, 213164, PR China

^b Institute of Machinery Manufacturing Technology, China Academy of Engineering Physics (CAEP), Mianyang, Sichuan, 621900, PR China

^c School of Mechanical Engineering and Rail Transit, Changzhou University, Changzhou, Jiangsu, 213164, PR China



ARTICLE INFO

Handling Editor: Dr P. Vincenzini

Keywords:

Mesoporous silica
Co-doping
Impregnation
Particle abrasive
Chemical mechanical polishing

ABSTRACT

Development of novel abrasive systems with functional activities and physicochemical properties are of great significance in the reactive oxygen species (ROS)-enhanced chemical mechanical polishing. In this work, Ce single-doped and Ce/Cu co-doped dendritic mesoporous silica nanoparticles (DMSNs), namely Ce–DMSNs and Ce/Cu–DMSNs, were produced via a simple impregnation and thermolysis procedure. The Ce and/or Cu species involved in DMSNs frameworks were characterized through X-ray diffractometry, infrared spectroscopy, scanning electron microscopy, energy dispersive spectrometry, transmission electron microscopy, X-ray photoelectron spectroscopy, and nitrogen adsorption/desorption techniques. We report the evolution of surface morphology and roughness, defects, peak-to-valley data, image surface area difference, and material removal efficiency during ROS-enhanced polishing experiments toward silica materials. All the pure, Ce single-doped, and Ce/Cu co-doped DMSNs abrasive systems offered nearly defect-free surfaces with close-to-atom scale roughness. It might be attributed to the “springlike effect” and “soft polishing/abrasion”, possibly originating from the low-modulus DMSNs carriers. Among these abrasives, the Ce/Cu co-doped DMSNs systems achieved an evident improvement in removal efficiency, especially under ultraviolet irradiation-assisted polishing conditions. The coexisted Ce(III)/Ce(IV) and Cu(I)/Cu(II) couples might be responsible for the effective production of ROS in photocatalysis and Fenton-like processes, thereby contributing to the Si–OH and Ce(III)–O–Si bonding formations. The role of the developed Ce/Cu co-doped DMSNs abrasive systems in ROS-enhanced polishing processes was discussed.

1. Introduction

Advanced oxidation processes (AOPs) [1,2] have emerged as powerful techniques tackling water, air, and soil pollution by the production and utilization of highly reactive oxygen species (ROS), such as hydroxyl radicals ($\bullet\text{OH}$), sulfate radicals ($\text{SO}_4^{\bullet-}$), superoxide anion radicals ($\bullet\text{O}_2^-$), etc. These ROS can cause the chemical bond breakage of recalcitrant organic compounds through the reactions such as electron transfer, hydrogen bonding addition, or substitution, ultimately oxidizing C and H into CO_2 and H_2O . Among these ROS, $\bullet\text{OH}$ radicals can be regarded as one of the most powerful oxidants ($E^\circ = 2.80 \text{ V}$) [1]. There are several reacting systems involved in ROS productions,

including photochemical and electrochemical oxidation, Fenton-related reactions, activated persulfate systems, ozone-involved systems, wet oxidation processes, ultraviolet (UV) or ultrasound or plasma treatments, etc. For example, the Fenton reaction [3,4] is an effective ROS generation system via the chain reactions, which typically employ H_2O_2 as radical precursors and $\text{Fe}^{2+}/\text{Fe}^{3+}$ (or other low-valent transition-metal complexes) as electron-donor/acceptor for triggering or terminating the generation of $\bullet\text{OH}$ radicals. In addition, photocatalysis oxidation is on the basis of the properties of semiconductors [5,6]. When the photocatalysts absorb photons with energy greater than or equal to the band gap, the photocatalytic reaction generates photogenerated electrons and holes that subsequently react with substances such as

* Corresponding author.

** Corresponding author.

*** Corresponding author.

E-mail addresses: cy.jpu@126.com (Y. Chen), wangchaohit@126.com (C. Wang), calcy@cczu.edu.cn (A. Chen).

H_2O_2 and O_2 in the system, yielding strongly oxidizing active free radicals (typically $\bullet\text{OH}$ and $\bullet\text{O}_2^-$).

Chemical mechanical polishing (CMP) technique commonly involves the chemical surface modification and subsequent mechanical material removal, aiming to achieve atomically smooth and defect-free surfaces. Recently, AOPs (typically photocatalysis and Fenton-related systems) and the as-generated ROS (typically $\bullet\text{OH}$ radicals) have been introduced into conventional CMP processes. Up to now, a series of Fenton (or photo-Fenton and electro-Fenton) reactions assisted CMP [4–15], Fenton-like reactions assisted CMP [16–18], photochemical (or photocatalytic) mechanical polishing (PCMP) [19–25], photocatalysis combined with Fenton reaction assisted CMP [26,27], photoelectrochemically mechanical polishing (PECMP) [28] techniques have been developed for improved polishing performance. It is noteworthy that these novel polishing methods can be collectively referred to as ROS (or free radical)-assisted CMP. Efficient material removal can be achieved by utilizing highly active groups for the oxidation and corrosion of hard and brittle materials (fused silica, silicon carbide, gallium nitride, etc.) coupled with the friction and wear of abrasive particles. Polishing results clearly indicate that ROS (or free radical)-assisted CMP can not only effectively improve removal efficiency but also achieve non-damage surfaces with atomic-level roughness. Importantly, ROS-assisted surface oxidation (or modification) is much effective and clean than traditional chemical oxidants such as sodium hypochlorite, potassium permanganate, potassium chromate, etc. Consequently, it is reasonable to believe that ROS-assisted CMP can be expected to develop into a clean, high-efficiency, and high-quality polishing technique.

In CMP practices, the surface quality and removal rate are a coupled result of the surface modification and mechanical removal. The type, structure, and property of abrasives play a crucial role in final polishing performance. The development of novel abrasive systems can be expected to provide valuable insights into the coordinating the contradiction between surface quality and removal efficiency during CMP. Thanks to the advancements of particle design and preparation technologies, a series of modified [29], doped [20,30–32], porous [33–35], core–shell structured [20,22–25,36–39], and irregular-shaped [40,41] abrasive systems have been proposed and applied in CMP, PCMP, electrochemical mechanical polishing (ECMP), etc. As confirmed by the experimental results, the synthetic abrasives with unique components and structures contributed to surface quality improvement and/or removal rate enhancement, possibly resulting from the regulation and optimization of the interfacial contact state and abrasion behavior between abrasives and surfaces.

Dendritic mesoporous silica nanoparticles (DMSNs) [42,43] have three-dimensional nanochannels and layered nanocavities, thus leading to a larger pore size, a higher pore volume, and more open channels than typical meso- SiO_2 materials such as SBA 15, MCM-41, etc. In particular, different nanoscale guests can be readily loaded into these channels as chemically active sites or transported through radial porous structures, thus creating novel composites with specific functional properties. In our previous work [16], the Cu-doped m SiO_2 abrasives were developed using a facile solvothermal method. CMP results on silica films revealed that the $\text{Cu}^{2+}/\text{H}_2\text{O}_2$ Fenton-like system contributed to the $\bullet\text{OH}$ production and thereby achieved an enhanced removal efficiency. Thus, introducing foreign cations into meso- SiO_2 frameworks may hold great potential in CMP practices. As one of the most popular CMP abrasives, SiO_2 nanoparticles have received widespread attentions in the past decades. For example, Lei and coworkers [44,45] prepared a series of Sm, Nd, Ce, or La-doped colloidal SiO_2 abrasives by a seed-induced growth method. And the enhanced removal rates toward sapphire substrates might be attributed to the solid-state chemical reactions between the doped SiO_2 abrasives and the reacted sapphire surfaces. To the best of our knowledge, the Ce/Cu co-doped colloidal SiO_2 or meso- SiO_2 abrasives have not been reported yet.

Inspired by previous works, herein we report some recent studies on

the design and synthesis of active and efficient abrasive systems toward ROS (or free radical)-assisted CMP. Herein, the uniform DMSNs synthesized by a typical oil–water biphasic stratification approach were single-doped with Ce species and co-doped with Ce/Cu species through a simple impregnation–calcination procedure. The Ce/Cu co-doped DMSNs (Ce/Cu–DMSNs) materials offered an improved polishing performance and an enhanced degradation activity by compared with those of pure and Ce single-doped DMSNs (Ce–DMSNs). Various analytical techniques, such as X-ray diffraction, Fourier transform infrared spectroscopy, Raman spectroscopy, transmission electron microscopy, scanning electron microscopy, energy-dispersive spectrometry mapping, nitrogen adsorption-desorption, X-ray photoelectron spectroscopy, atomic force microscopy, etc., are used in this work. A possible polishing mechanism toward the developed Ce/Cu–DMSNs abrasive systems is proposed according to the synergistic effect of ROS-enhanced surface modification and soft abrasion-assisted material removal.

2. Experimental section

2.1. Materials and reagents

All chemical reagents including cerium nitrate hexahydrate ($\text{Ce}(\text{NO}_3)_3 \cdot 6\text{H}_2\text{O}$, AR), hydrated copper nitrate ($\text{Cu}(\text{NO}_3)_2 \cdot 3\text{H}_2\text{O}$, AR), cetyltrimethylammonium bromide (CTAB, AR), tetraethyl orthosilicate (TEOS, AR), triethanolamine (TEA, AR), *n*-hexane (C_6H_{14} , AR), ethanol ($\text{C}_2\text{H}_6\text{O}$, AR), hydrogen peroxide (H_2O_2 , 30 wt%, AR), tetracycline (TC, CP) were purchased from Shanghai Chemical Reagent Co., Ltd. (China) and used as received without further purification. Deionized (DI) water was used throughout the experimental processes.

2.2. Synthesis of DMSNs, Ce–DMSNs, Cu–DMSNs, and Ce/Cu–DMSNs

The DMSNs with a particle size of 70–80 nm were prepared via the biphasic stratification approach [46] with a little modification. Briefly, 0.18 g of TEA and 1.0 g of CTAB were added to 60 mL of DI water and magnetically stirred (150 r/min), coupled with a standard Teflon-coated stirring bar with a length of 3 cm at 60 °C for 60 min in a round-bottomed flask. Then, a mixture of 7.44 mL of TEOS and 13.8 mL of *n*-hexane was charged into the water–CTAB–TEA system, and the solution was kept at 60 °C in an oil bath under magnetic stirring (150 r/min). After 24 h, the upper oil phase was removed carefully, and the resulting products were collected by repeated centrifugation (10000 r/min) and washed for several times with DI water and ethanol to remove the residual reactants. The collected samples were dried in an oven at 75 °C, followed by calcination in a muffle furnace at 650 °C for 2 h to remove the CTAB templates. Finally, the DMSNs products were obtained for next experiments.

The Ce/Cu–DMSNs were prepared by two-step impregnation and thermolysis procedures. A typical synthesis was described as following. Generally, the as-made DMSNs (0.30 g) were impregnated with the mixture containing $\text{Ce}(\text{NO}_3)_3 \cdot 6\text{H}_2\text{O}$ (0.21 g, 0.25 mmol), $\text{Cu}(\text{NO}_3)_2 \cdot 3\text{H}_2\text{O}$ (0.12 g, 0.25 mmol), and ethanol (20 mL) at room temperature, followed by ultrasonication for 10 min. Then the suspension was aged for 2 h under magnetic stirring (200–300 r/min). Subsequently, the mixture was heated to 45 °C in an oil bath for the complete evaporation of ethanol. Finally, the solids were calcined in a muffle furnace at 550 °C for 2 h. For comparison, Ce–DMSNs and Cu–DMSNs were synthesized by following the similar procedure as described above, except using the $\text{Ce}(\text{NO}_3)_3 \cdot 6\text{H}_2\text{O}$ (0.42 g, 0.50 mmol) and the $\text{Cu}(\text{NO}_3)_2 \cdot 3\text{H}_2\text{O}$ (0.24 g, 0.50 mmol) precursors, respectively.

2.3. Structure characterization

Field emission scanning electron microscopy (FESEM) and O, Ce, and/or Cu elemental mapping images were obtained using a ZEISS SUPRA-55 electron microscope equipped with embedded energy

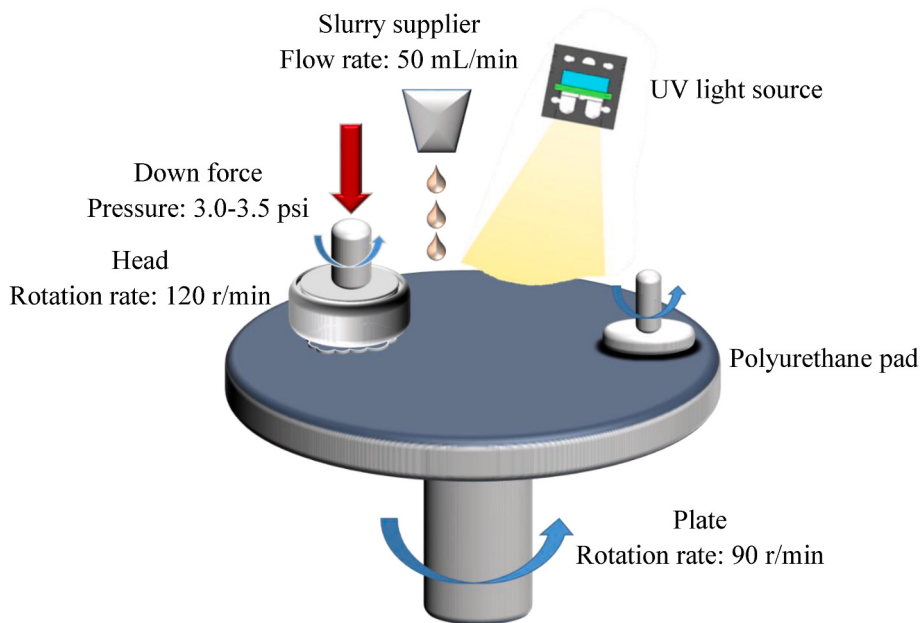


Fig. 1. Schematic view of the polishing setup.

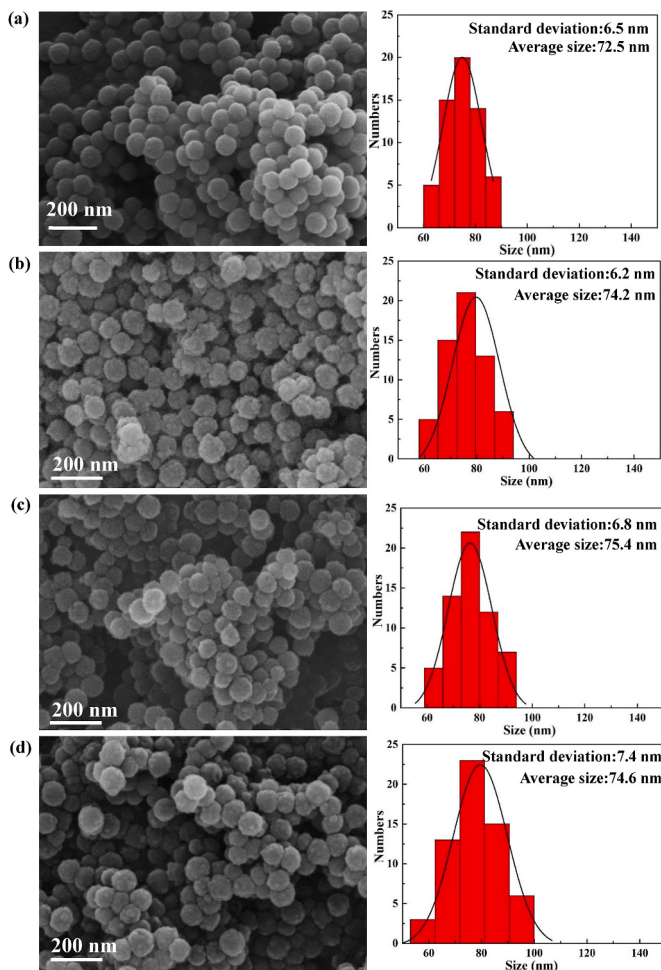


Fig. 2. SEM images and particle-size distribution plots of (a) DMSNs, (b) Ce–DMSNs, (c) Cu–DMSNs, and (d) Ce/Cu–DMSNs products.

dispersive spectrometer (EDS) system and operated at an accelerating voltage of 15 kV. The samples were coated with a thin layer of gold before SEM observations. Transmission electron microscopy (TEM) images were obtained using a JEOL JEM-2100 electron microscope, operating at an accelerating voltage of 120 kV. Prior to the analysis, the samples were dispersed into ethanol with ultrasonic treatment for 10 min, and a drop of the suspension was placed on a carbon-coated copper grid and dried in air. Nitrogen adsorption-desorption isotherms were measured using a Micromeritics TriStar 3020 instrument at 77 K. The specific surface areas were calculated by the Brunauer–Emmett–Teller (BET) method, and the pore-size distributions were estimated from the adsorption branch data using the Barrett–Joyner–Halenda (BJH) model. Fourier transform infrared spectroscopy (FT-IR) analyses were performed on a Nicolet Avatar-370 spectrometer. X-ray diffraction (XRD) analyses were performed on a Rigaku D/Max 2500 PC diffractometer using $\text{Cu-K}\alpha$ radiation source ($\lambda = 1.54056 \text{ \AA}$). The chemical states and compositions of the samples were explored using an X-ray photoelectron spectrometer (XPS, PHI-5000 VersaProbe III, ULVAC-PHI) equipped with a monochromatic Al $\text{K}\alpha$ ($h\nu = 1486.6 \text{ eV}$) radiation source. The binding energies were calibrated using the C 1s reference peak at 284.8 eV.

2.4. Polishing experiments

All polishing tests were performed on a precision polisher (Tegra-Force-1-TrgraPol-15, Struers, Denmark) coupled with a porous polyurethane pad (MD-Chem, Struers). Thermally grown SiO_2 wafers (ca. 1.2 μm in oxide layer thickness) with a size of ca. 20 mm \times 20 mm \times 0.5 mm (length \times width \times thickness) were used as processing targets. In UV radiation-assisted PCMP processes, a 250 W UV lamp (wavelength 365 nm) served as an UV light source, and placed ca. 30 cm above the polishing pad. The diagram of the experimental device is shown in Fig. 1. The process conditions were as follows: polishing pressure of 3.0–3.5 psi, head rotation speed of 120 r/min, plate rotation speed of 90 r/min, slurry flow rate of 50 mL/min, polishing time of 2 min. Typically, the slurries were composed of abrasive particles (DMSNs, Ce–DMSNs, or Ce/Cu–DMSNs) with a solid content of 1.0 wt%, H_2O_2 (1.0 wt%), PVP (1.0 wt%), and DI water. And the slurry pH was adjusted to 8.0–8.5 using 0.1 M NaOH. The slurries were continuously stirred to achieve uniformly dispersed suspensions. Prior to PCMP experiments, the

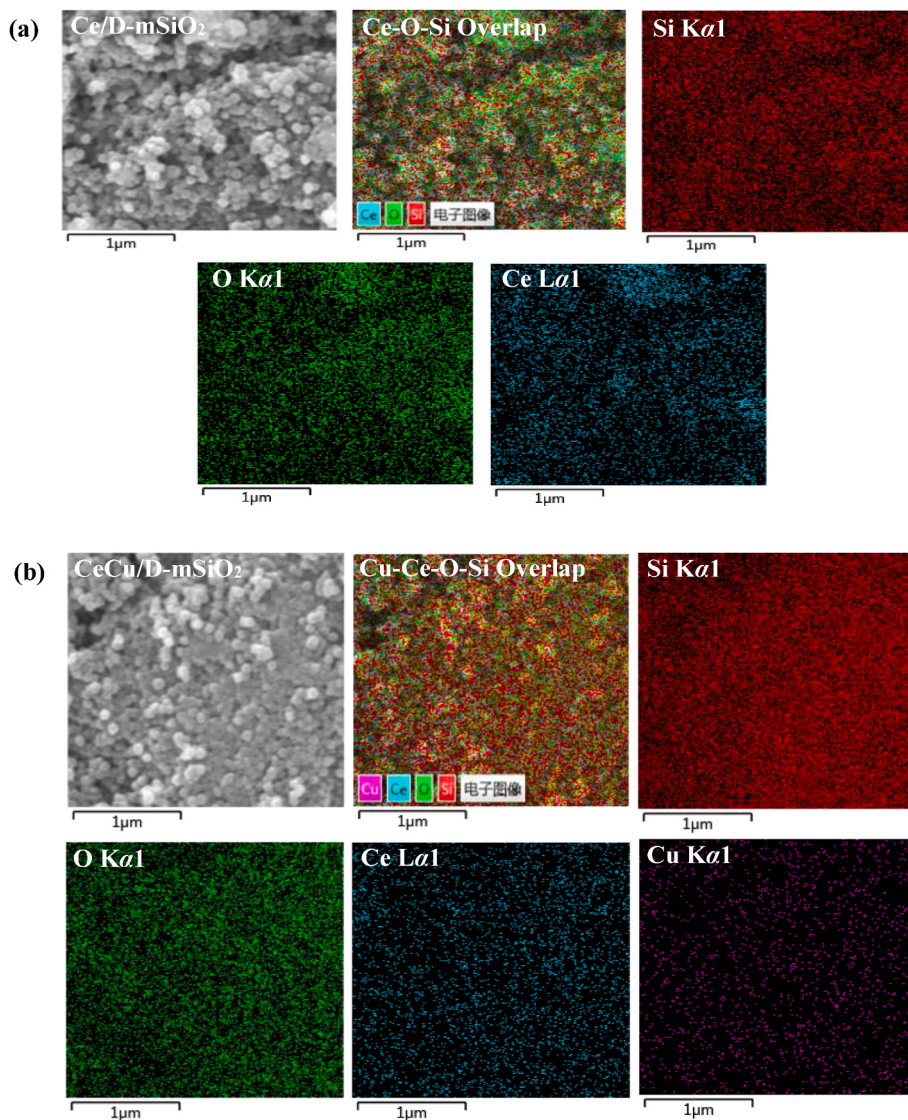


Fig. 3. SEM-EDS mapping images of (a) Ce–DMSNs and (b) Ce/Cu–DMSNs.

polishing slurries were also treated with UV light irradiation for 10 min.

After polishing, the workpieces were rinsed immediately by ultrasonication with ethanol, acetone, and DI water to remove the adhered abrasive particles and other residues from the surfaces. The surface morphologies of the substrates before and after finishing were evaluated using a non-contact 3D optical profilometer (Contour GT, Bruker) and an atomic force microscope (AFM, Nanoman VS coupled with a Dimension V controller, Veeco, currently Bruker) in tapping mode. Commercial silicon probes (Tap300Al-G, obtained from BudgetSensors) were used in all AFM measurements. The typical tip radius, resonance frequency, and spring constant are ~10 nm, 300 kHz, and 40 N/m, respectively. And the scan speed, scan area, and scan resolution were fixed at 1.0 Hz, 5.0 μm × 5.0 μm, and 512 px × 512 px, respectively. AFM measurement positions were randomly selected from the surfaces in order to ensure the credibility of the roughness determinations. In addition, the finished surfaces and the abrasive particles in used slurries were also examined by SEM observations (Regulus 8100, Hitachi).

The weight of the workpiece before and after polishing was measured using an electric balance (XS105, Mettler Toledo) with a 0.01 mg resolution to determine the material removal rate (*MRR*), as shown in equation (1).

$$MRR = \Delta m / \rho s t \quad (1)$$

where Δm is the weight loss of the workpiece, ρ is the SiO_2 layer density (ca. 2.2 g/cm³), s is the workpiece surface area, and t is the polishing time. In this work, the provided *MRR* and roughness data were determined by averaging values obtained from the three repeated tests.

3. Results and discussion

3.1. Structural and physicochemical properties

Fig. 2 shows the FESEM images and the corresponding particle-distribution plots of DMSNs, Ce–DMSNs, Cu–DMSNs, and Ce/Cu–DMSNs samples. In this work, the average diameter and standard deviation of the particles were determined via the Nano Measurer Software (V1.2) by counting 60–80 nanospheres for statistical appreciations. As shown in **Fig. 2a**, the bare DMSNs have relatively smooth appearances and uniform spherical morphologies with an average particle size of 72.0 ± 6.5 nm. After doping and co-doping with Ce and/or Cu species, the Ce–DMSNs (**Fig. 2b**), Cu–DMSNs (**Fig. 2c**), and Ce/Cu–DMSNs (**Fig. 2d**) still maintain the initial spherical shapes, also indicating the good structural stability of DMSNs during the synthesis procedures. In addition, the Ce–DMSNs, Cu–DMSNs, and Ce/Cu–DMSNs reveal comparable diameters with narrow particle size-distributions, namely, 74.2 ± 6.2 nm, 75.4 ± 6.8 nm, and 74.6 ± 7.4

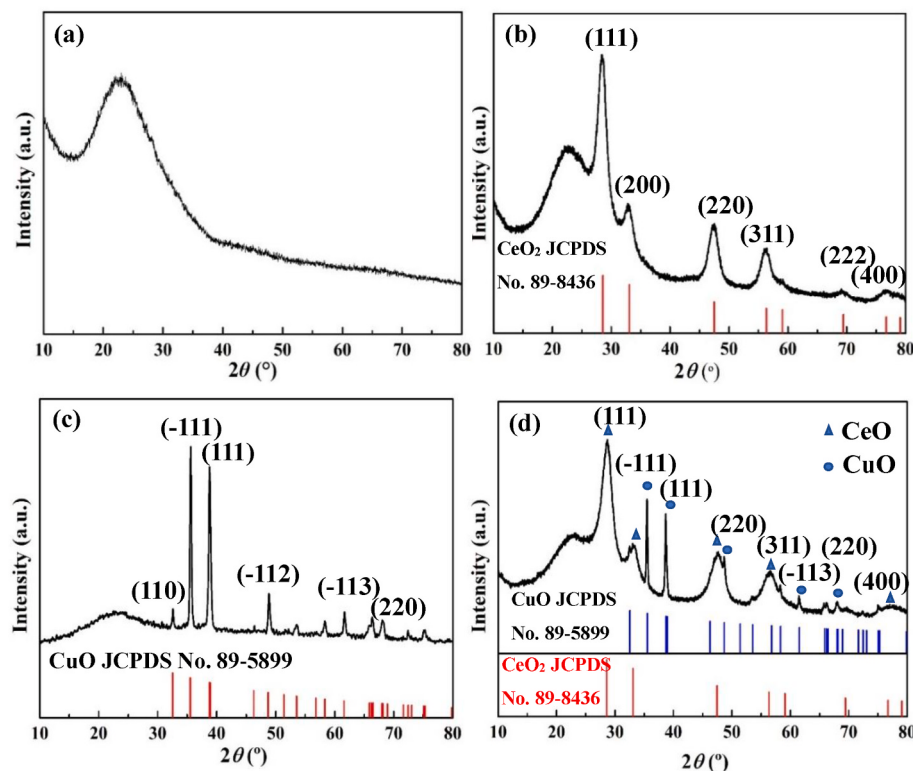


Fig. 4. XRD patterns of (a) DMSNs, (b) Ce–DMSNs, (c) Cu–DMSNs, and (d) Ce/Cu–DMSNs samples.

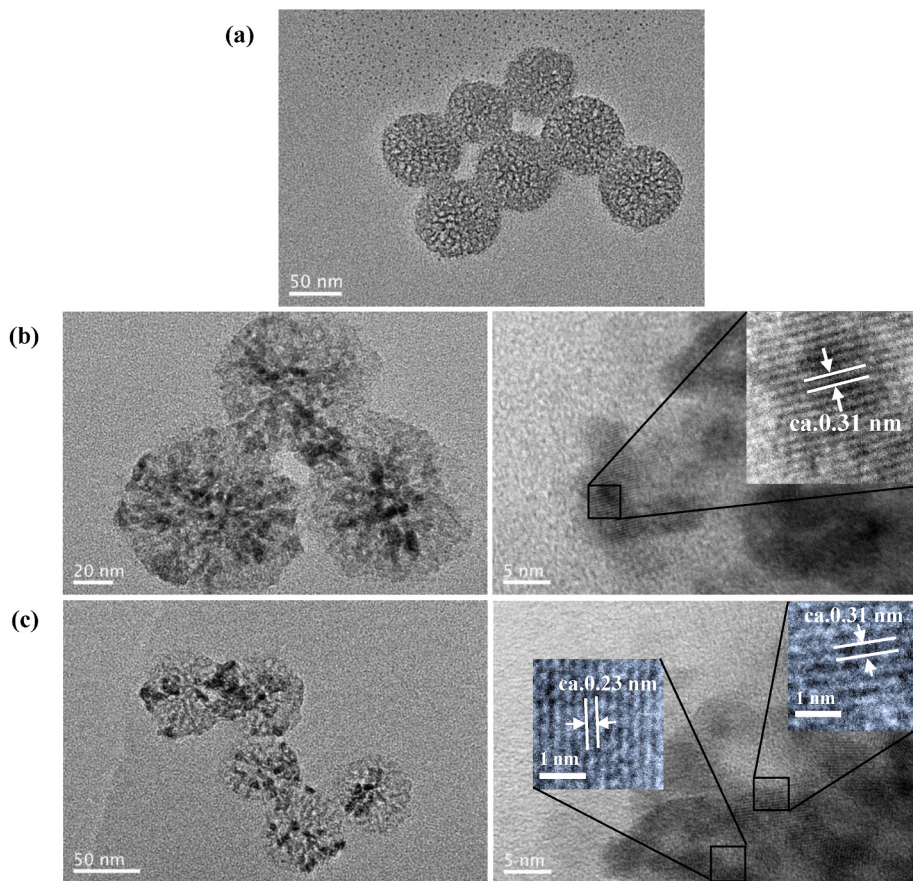


Fig. 5. TEM images of (a) DMSNs, (b) Ce–DMSNs, and (c) Ce/Cu–DMSNs samples.

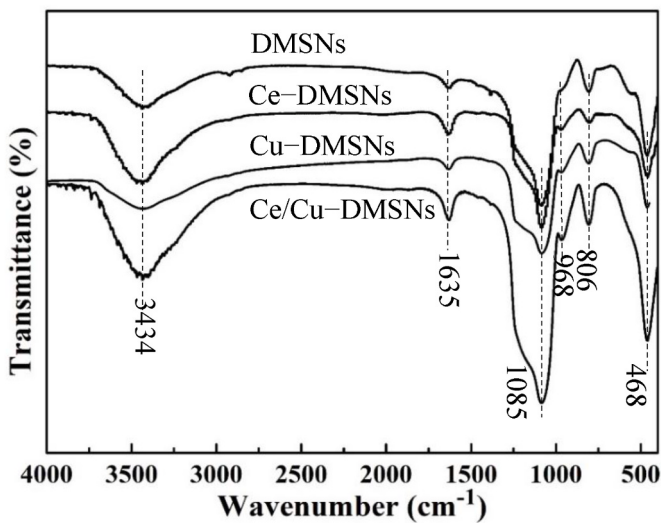


Fig. 6. FT-IR spectra of DMSNs, Ce-DMSNs, Cu-DMSNs, and Ce/Cu-DMSNs.

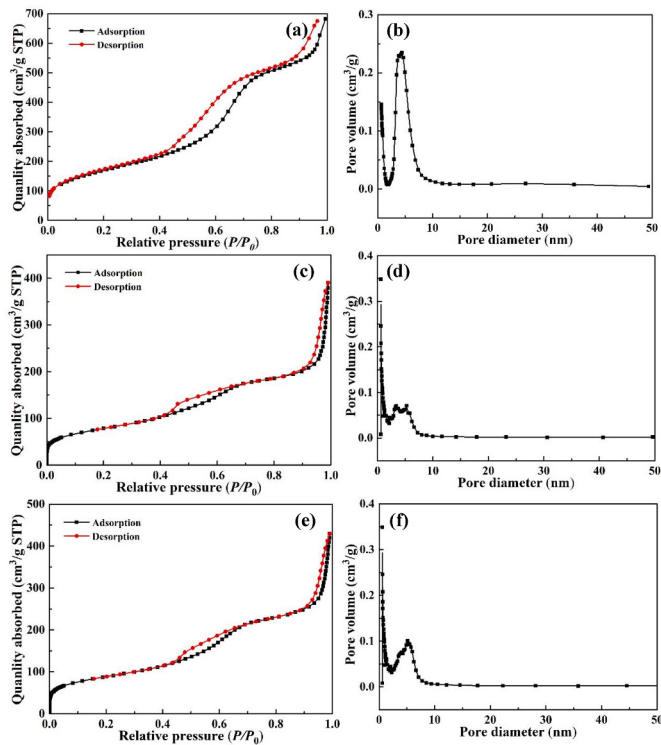


Fig. 7. Nitrogen adsorption-desorption isotherms and the corresponding pore-size distributions of (a, b) DMSNs, (c, d) Ce-DMSNs, and (e, f) Ce/Cu-DMSNs samples.

nm. Furthermore, the relatively rough surfaces and slightly increased sizes further suggest that there are some Ce and/or Cu oxide species grafted at DMSNs surfaces.

The SEM-EDS analyses (Fig. 3) were also employed to analyze the chemical compositions of the Ce-DMSNs and Ce/Cu-DMSNs samples, identifying that the elements of Si, O, Ce, and Cu (for Ce/Cu-DMSNs) were electrodeposited. As confirmed by the corresponding EDS elemental mapping images, the Si (red), O (green), Ce (blue), and Cu (purple, for Ce/Cu-DMSNs) elements are homogeneously distributed in the Ce-DMSNs (Fig. 3a) and Ce/Cu-DMSNs (Fig. 3b) particles. The presented EDS mapping data verify the uniform introduction of Ce and/or Cu species into the DMSNs matrixes using the

impregnation–calcination approach.

The crystalline and amorphous nature of the DMSNs, Ce-DMSNs, Cu-DMSNs, and Ce/Cu-DMSNs samples were analyzed by powder XRD patterns. For bare DMSNs (Fig. 4a), only a broad peak located at ca. $2\theta = 21.8^\circ$ can be observed, indicating the presence of amorphous (non-crystalline) silica materials [47,48]. All three doped DMSNs samples also reveal the amorphous diffraction peaks, which can be attributed to the involved amorphous DMSNs frameworks. For Ce-DMSNs (Fig. 4b), the diffraction peaks located at ca. $2\theta = 28.3^\circ, 32.8^\circ, 47.4^\circ, 56.1^\circ, 69.1^\circ$, and 76.5° can be indexed to the characteristic (111), (200), (220), (311), (222), and (331) reflections of cubic fluorite-type phase CeO_2 materials [49,50]. In the case of Cu-DMSNs (Fig. 4c), the sharp diffraction peaks at ca. $2\theta = 32.6^\circ, 35.5^\circ, 38.8^\circ, 48.8^\circ$, and 61.6° , corresponding to the (110), (−111), (111), (−112), and (−113) crystal planes of monoclinic CuO phase [51,52], supporting the presence of the well-crystallized CuO . Furthermore, the characteristic XRD diffraction peaks of both cubic phase CeO_2 and monoclinic phase CuO can be clearly observed from Fig. 4d, indicating the coexistence of CeO_2 and CuO nanocrystals in Ce/Cu-DMSNs.

More structural characterizations on DMSNs, Ce-DMSNs, and Ce/Cu-DMSNs were performed using TEM observations. By comparison with initial DMSNs (Fig. 5a), there are no significant changes in particle morphology, particle size, and pore structure for the Ce-DMSNs (Fig. 5b) and Ce/Cu-DMSNs (Fig. 5c) samples. In addition, some black dots can be found at the Ce and/or Cu-doped DMSNs surfaces, implying the formation of CeO_2 and/or CuO nanoparticles [53]. For the Ce-DMSNs, high-resolution TEM (HRTEM) image gives the interplanar spacing of 0.31 nm, corresponding to the exposed (111) plane of CeO_2 . In the case of Ce/Cu-DMSNs, two sets of lattice fringes with spacing values of 0.31 and 0.23 nm are tracked, which can be indexed to the (111) plane of CeO_2 and (111) facet of CuO [54]. The results of HRTEM investigations are in line with the XRD analyses.

Fig. 6 shows the FT-IR spectra of the DMSNs, Ce-DMSNs, Cu-DMSNs, and Ce/Cu-DMSNs samples. The intense IR signal centered at ca. 3434 cm^{-1} can be ascribed to the stretching vibration of the sialon and −OH groups [55]. The H–O–H bending vibration mode appeared at ca. 1635 cm^{-1} may be attributed to the adsorption water molecules within the DMSNs-involved materials [49]. The characteristic IR bands at ca. 468 cm^{-1} , 806 cm^{-1} , and 1083 cm^{-1} can be assigned to the in-plane bending of Si–O–Si, the symmetric vibration of Si–O, and the stretching vibration of Si–O in the Si–O–Si structure [56], respectively. Furthermore, the IR signals at ca. 1083 cm^{-1} for the doped DMSNs samples are evident broader than that of undoped ones, which can be responsible for the incorporation of Ce and/or Cu ions into the silica frameworks [57]. Moreover, the IR band near 968 cm^{-1} can be ascribed to the Si–OH vibrations. As reported in literatures [58,59], the increase in the intensity of this signal possibly resulted from the incorporation of heteroatom into silica materials. Consequently, the increased IR band intensity at ca. 968 cm^{-1} can be attributed to the framework Si–O–M (M: Ce and/Cu) stretching vibrations for the Ce and/or Cu doped DMSNs samples. The results of FT-IR analyses further suggest that a portion of Ce and/or Cu species may be incorporated into the silica frameworks of mesoporous Ce-DMSNs, Cu-DMSNs, and Ce/Cu-DMSNs, even though it is hard to quantify the incorporated amounts in the silicate frameworks. Nevertheless, the characteristic IR signals on CeO_2 and CuO cannot be clearly detected. Many available literatures [57–59] have reported the similar results on metal-incorporated mesoporous silica materials, such as Al-MCM-41, Cu/Al-MCM-41, Cu-SBA-15, La-SBA-15, etc.

To determine the textural features of DMSNs, Ce-DMSNs, and Ce/Cu-DMSNs, the low-temperature N_2 adsorption–desorption isotherms and pore-size distributions were investigated, as shown in Fig. 7. According to International Union of Pure and Applied Chemistry classification, all isotherms (Fig. 7a–c, e) show a typical Type IV model with a H2/H3-type hysteresis loop at a high relative pressure, indicating the presence of dendritic-like mesopores [46]. The BET surface area and

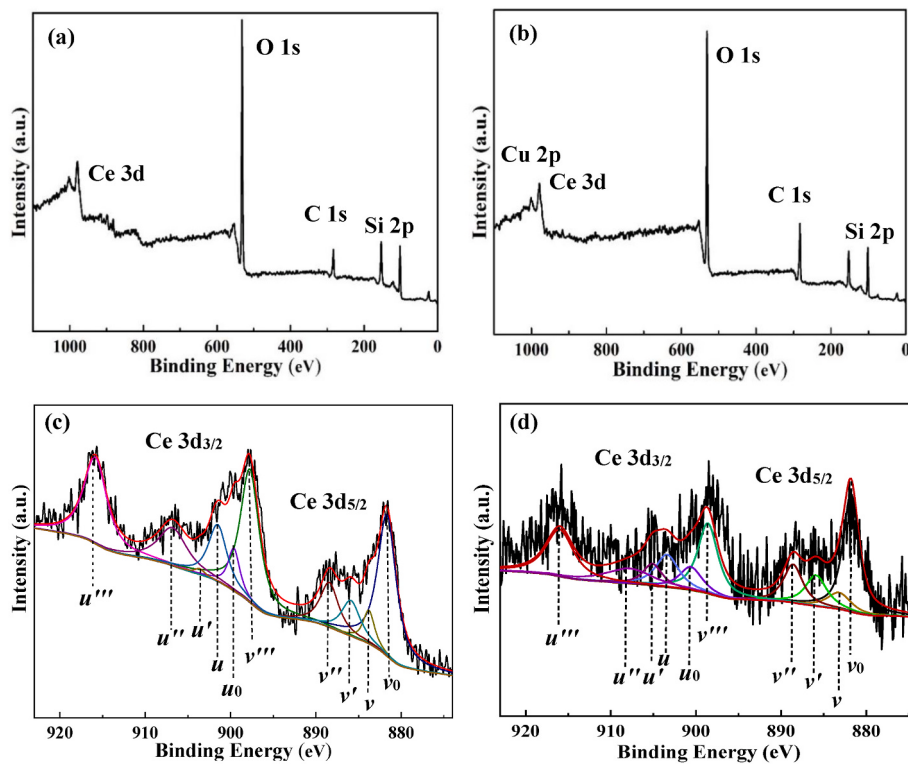


Fig. 8. Survey and Ce 3d XPS spectra of (a, c) Ce-DMSNs and (b, d) Ce/Cu-DMSNs.

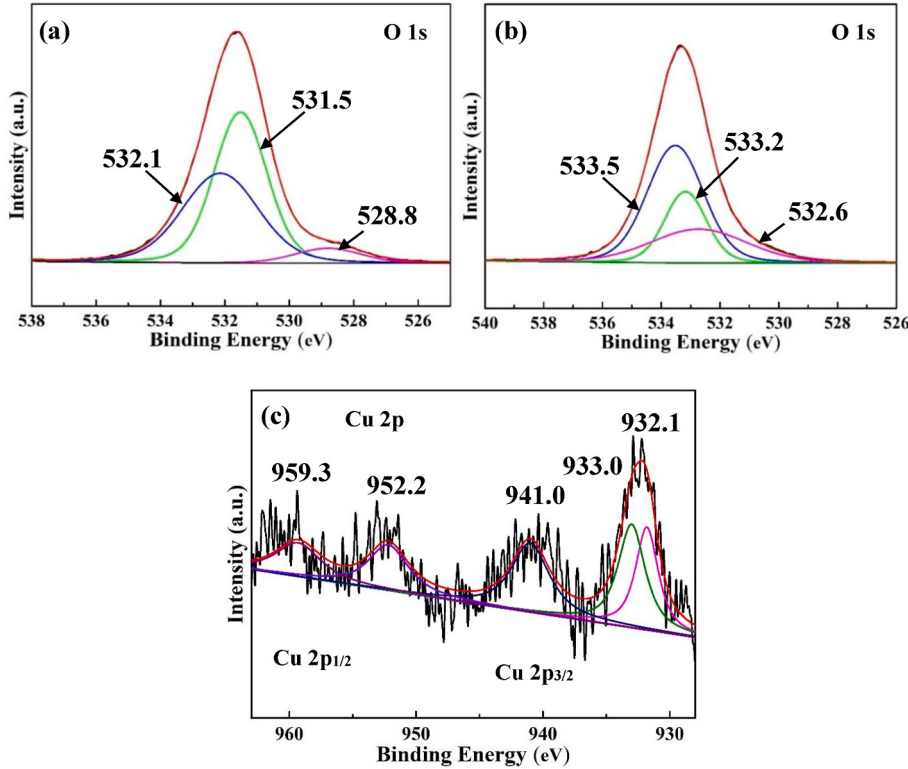


Fig. 9. O 1s and Cu 2p XPS spectra (a) Ce-DMSNs and (b, c) Ce/Cu-DMSNs.

pore volume of the blank DMSNs were determined to be $605.8 \text{ m}^2/\text{g}$ and $1.18 \text{ cm}^3/\text{g}$, respectively. However, the Ce-DMSNs and Ce/Cu-DMSNs are shown to suffer a considerable loss on surface areas (265.9 and $299.7 \text{ m}^2/\text{g}$) and pore volumes (0.60 and $0.66 \text{ cm}^3/\text{g}$). It may be

attributed to the blocking of the pores of DMSNs matrixes by CeO_2 and/or CuO nanoparticles and their aggregates [57–60]. It also suggests that there are some CeO_2 and/or CuO nanocrystals formed within the DMSNs mesochannels. Fig. 7b-d, f shows the BJH pore-size distributions

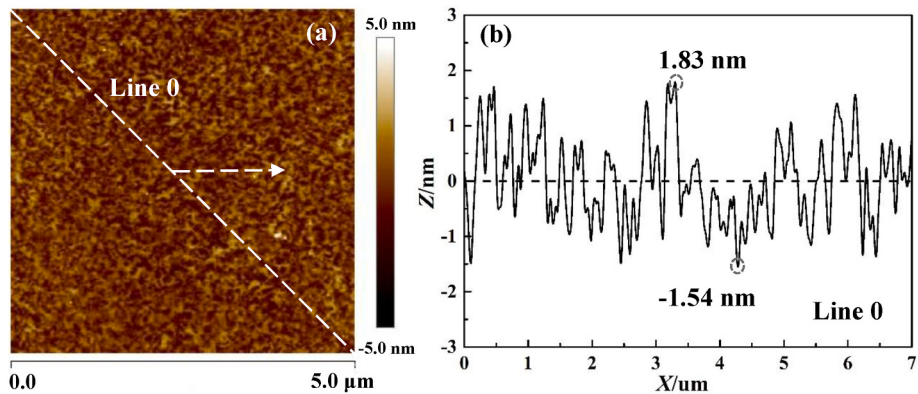


Fig. 10. AFM analyses on the as-received silica surface (a) height image and (b) line-scan trace.

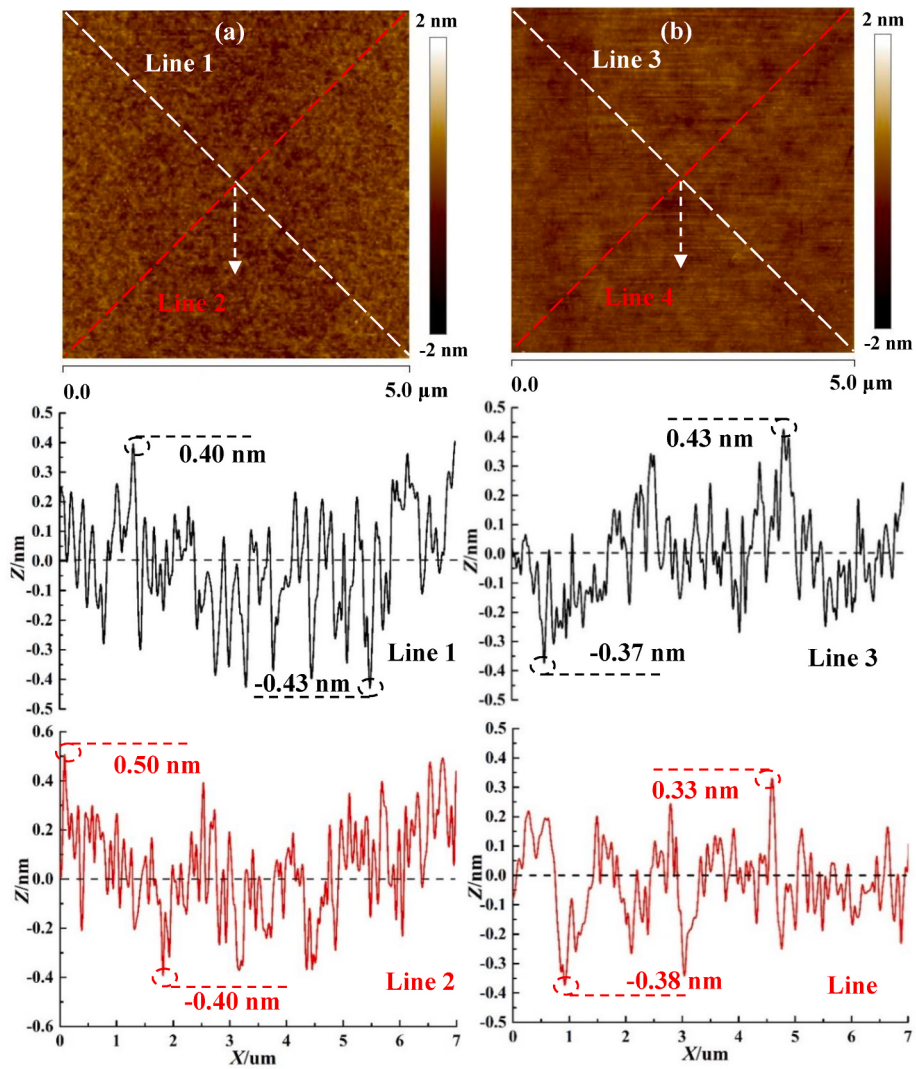


Fig. 11. AFM height images and the line-scan traces of the surfaces after CMP with (a) DMSNs and (b) Ce–DMSNs.

of the pure and doped DMSNs samples, as determined from the adsorption branch data. All samples exhibit a good mesoporous structural ordering and a narrow pore-size distribution. In addition, the DMSNs, Ce–DMSNs, and Ce/Cu–DMSNs have a comparable average pore diameter, namely, 9.2, 9.0, and 8.9 nm.

The chemical composition and valence/oxidation state on the obtained samples were further tracked using XPS investigations. The

survey XPS spectra confirm the presence of C, Si, O, Ce, and/or Cu elements on the Ce–DMSNs (Fig. 8a) and Ce/Cu–DMSNs (Fig. 8b) surfaces. Ce 3d XPS spectrum commonly demonstrates complex features, possibly resulting from the hybridization with ligand orbitals and fractional occupancy of the valence 4f orbitals. The complex Ce 3d spectra of the Ce–DMSNs (Fig. 8c) and Ce/Cu–DMSNs (Fig. 8d) materials were deconvoluted into five pairs of peaks. Herin, two sets of spin orbit

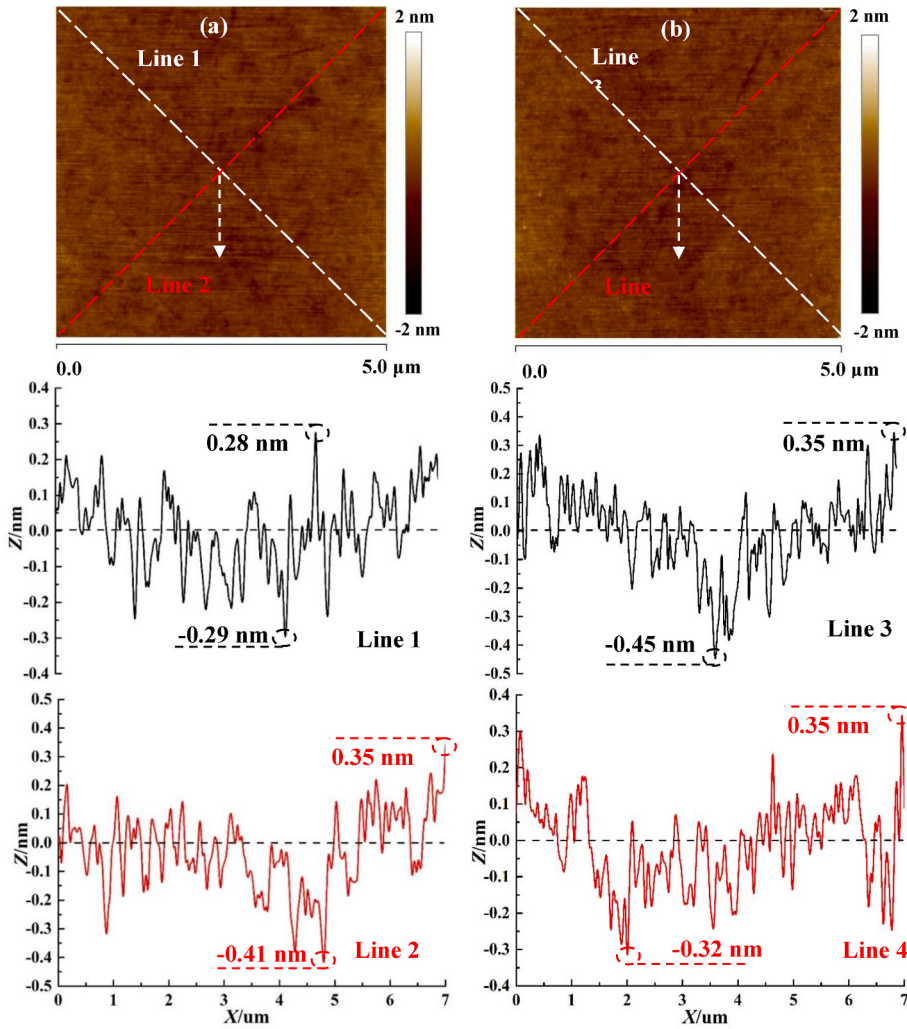


Fig. 12. Typical AFM height images and the corresponding line-scan traces of the surfaces after (a) CMP and (b) PCMP with Ce/Cu–DMSNs.

polymorphisms (Ce 3d_{3/2} and Ce 3d_{5/2}) represent *u* and *v*, respectively. For Ce–DMSNs (Ce/Cu–DMSNs) samples, three pairs of peaks centered at ca. 883.8 (883.2) and 901.5 (903.4) eV, 888.4 (888.6) and 906.8 (907.8) eV as well as 897.8 (898.6) and 915.9 (916.0) eV can be ascribed to Ce 3d⁹4 f² O 2p⁴ (*v*, *u*), Ce 3d⁹4 f¹ O 2p⁵ (*v'*, *u'*) and Ce 3d⁹4 f⁰ O2p⁶ (*v''*, *u''*) of Ce (IV) species, respectively. The other two pairs of peaks at 881.7 (881.8) and 899.6 (900.6) eV as well as 885.9 (885.9) and 903.6 (905.1) eV, labeled as *v*₀, *u*₀ and *v'*, *u'*, can be assigned to the Ce(III) species with Ce 3d⁹4 f² O 2p⁵ and Ce 3d⁹4 f¹ O 2p⁶ final states [61]. These results confirm that two valence states of Ce(IV) and Ce(III) coexist in Ce- and Ce/Cu-doped DMSNs materials. Furthermore, the Ce (III) concentration can be estimated through semi-quantitative calculation using equation (4) [62–64]. And the oxygen vacancy (Vo) content in CeO₂ can be calculated according to equation (5) [62,64]. The Ce(III) and Vo concentrations of Ce/Cu–DMSNs are 39.5 % and 9.9 %, respectively, which are higher than those of Ce–DMSNs (32.8 % and 8.2 %).

$$\text{Ce(III)\%} = A [\text{Ce(III)}] / A [\text{Ce(III)} + \text{Ce(IV)}] \quad (4)$$

$$\text{Vo\%} = 1 - (3[\text{Ce(III)}] + 4[\text{Ce(IV)}]) / 4 \quad (5)$$

The O 1s XPS analyses were also performed to determine the different types of oxygen species in the synthesized materials. Three different O 1s peaks can be noticed in the Ce–DMSNs (Fig. 9a) and Ce/Cu–DMSNs (Fig. 9b) samples. As proposed in literatures [65,66], the binding energy centered at 528.8–532.6 eV can be assigned to the

lattice oxygen (such as O²⁻ species) of the metal oxides, while the shoulder peak located at 531.5–533.2 eV can be attributed to oxygen vacancies or chemisorbed oxygen species. Moreover, the binding energy at 532.1–533.5 eV can be associated with other oxygen species, including weakly bounded water molecules.

It is commonly recognized that CuO possess characteristic high-intensity shake-up satellites [67–69]. Fig. 9c presents the Cu 2p XPS spectrum of Ce/Cu–DMSNs samples. Herin, the Cu 2p_{3/2} and 2p_{1/2} core-levels peaks are located at ca. 933.0 and 952.2 eV, respectively. The recorded core level spectrum also shows the signature of the presence of shake-up satellites. The peak located at ca. 941.0 eV is the signature for the presence of satellite peak of Cu 2p_{3/2}, and the satellite peak for the Cu 2p_{1/2} is located at ca. 959.3 eV. Moreover, the peak at 932.1 eV can be ascribed to the reduced copper species (Cu(I) and/or Cu⁰) [61, 67–69]. Nevertheless, the presence of Cu⁰ should be ignored in this work. Consequently, both Cu(II) and Cu(I) oxidation states may also coexist in Ce/Cu–DMSNs samples.

3.2. Degradation activities

The catalytic activities and ROS production efficiencies of DMSNs, Ce–DMSNs, and Ce/Cu–DMSNs materials were evaluated from the degradation tests toward TC. The experiments were performed on a GHX-2 photochemical reaction apparatus (Yangzhou University Town Science and Education Instrument Co., Ltd.) equipped with a water-cooled 300 W Xeon lamp. In a typical experiment, a round bottom

Table 1

Surface characteristics of the substrates after CMP and PCMP with different DMSNs-involved abrasive systems.

DMSNs (CMP)	<i>R_a</i> (nm) ^a	<i>R_q</i> (nm) ^b	<i>R_z</i> (nm) ^c	Surface Area Difference (%) ^d
Run 1	0.158	0.206	0.317	0.00687
Run 2	0.173	0.234	0.332	0.00598
Run 3	0.170	0.228	0.330	0.00652
Average	0.167 ± 0.008	0.223 ± 0.015	0.326 ± 0.008	0.00645 ± 0.00044
Ce–DMSNs (CMP)	<i>R_a</i> (nm)	<i>R_q</i> (nm)	<i>R_z</i> (nm)	Surface Area Difference (%)
Run 1	0.124	0.154	0.176	0.00350
Run 2	0.118	0.143	0.170	0.00343
Run 3	0.126	0.158	0.174	0.00372
Average	0.123 ± 0.004	0.152 ± 0.008	0.173 ± 0.003	0.00355 ± 0.00015
Ce/Cu–DMSNs (CMP)	<i>R_a</i> (nm)	<i>R_q</i> (nm)	<i>R_z</i> (nm)	Surface Area Difference (%)
Run 1	0.143	0.172	0.182	0.00349
Run 2	0.149	0.182	0.187	0.00421
Run 3	0.132	0.163	0.181	0.00305
Average	0.141 ± 0.009	0.172 ± 0.010	0.183 ± 0.003	0.00358 ± 0.00059
Ce/Cu–DMSNs (PCMP)	<i>R_a</i> (nm)	<i>R_q</i> (nm)	<i>R_z</i> (nm)	Surface Area Difference (%)
Run 1	0.121	0.142	0.150	0.00291
Run 2	0.114	0.138	0.140	0.00273
Run 3	0.126	0.152	0.157	0.00334
Average	0.120 ± 0.006	0.144 ± 0.007	0.149 ± 0.009	0.00299 ± 0.00031

^a Arithmetic average of the absolute values of the surface height deviations measured from the mean plane.

^b Root-mean-square average of height deviations taken from the mean image data plane.

^c Average difference in height between the highest peaks and valleys relative to the mean plane.

^d Difference between the image's 2D surface area and 3D projected surface area.

flask containing a mixture of 25 mg photocatalyst and 250 mL TC solution (20 mg/L) was placed ca. 10 cm from the light source. First, the suspension was magnetically stirred for 60 min in the dark environment at room temperature, ensuring the adsorption/desorption equilibrium between the TC and DMSNs-based particles. Then, 1.0 mL of H₂O₂ solution was added into the reactor. After that, the suspension was illuminated with constant stirring, and 5 mL aliquots were collected every 10 min, followed by centrifugation (8000 rpm) to remove the catalyst particles. To determine the concentration of residual TC, the supernatant was analyzed using an UV-vis spectrophotometer (722, JINGHUR Instruments) at the maximum absorption wavelength of TC ($\lambda_{\text{max}} \approx 356$ nm). The degradation efficiency (η) was evaluated by measuring the change of absorbance via the following equation (2).

$$\eta = (1 - C_t / C_0) \times 100\% \quad (2)$$

Herein, C_0 is the initial concentration of TC, and C_t is the concentration of TC after degradation reaction. At a low TC content and the weak adsorption, the degradation reaction kinetics generally follow the Langmuir–Hinshelwood Kinetic model. And the reaction rate (k) was also determined using the following equation (3).

$$\ln(C) = -kt + \ln(C_0) \quad (3)$$

where k is the pseudo-first-order reaction rate constant (min⁻¹) and t is the reaction time. These procedures were triplicated for all DMSNs, Ce–DMSNs, and Ce/Cu–DMSNs samples.

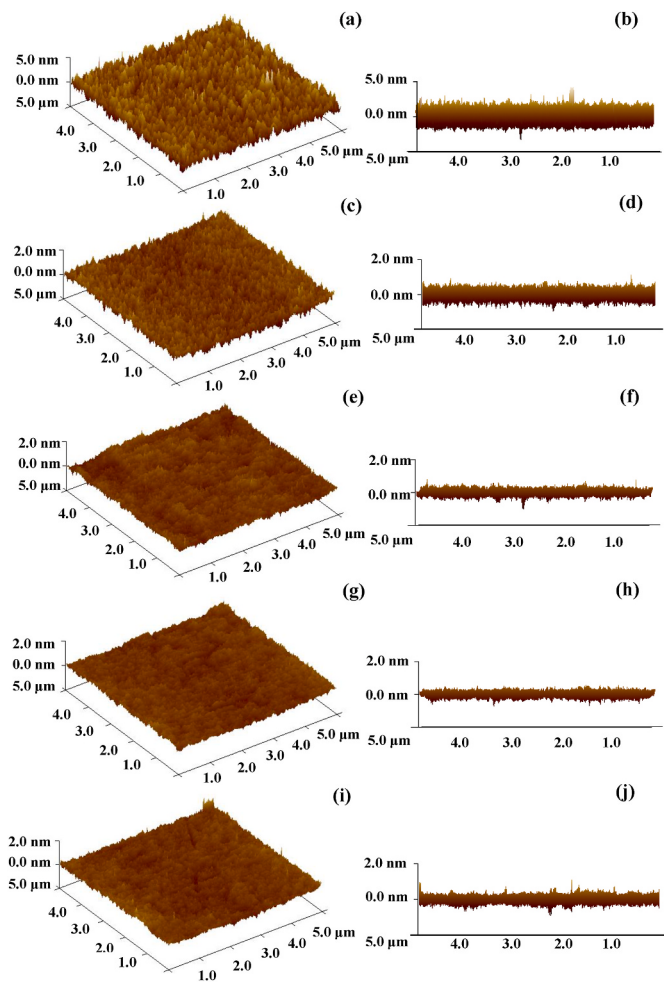


Fig. 13. 3D-AFM images and the corresponding lateral views of the substrates (a, b) before and after (c, d) CMP with DMSNs, (e, f) CMP with Ce–DMSNs, (g, h) CMP with Ce/Cu–DMSNs, and (i, j) PCMP with Ce/Cu–DMSNs.

3.3. Polishing performances

3.3.1. Surface quality

The topographical changes of the surfaces before and after polishing were explored by AFM analyses, including two-dimensional (2D) height images, three-dimensional (3D) oblique images, lateral views, line-scan traces, surface area difference (SAD), etc. The lower color contrast ratio in height images commonly suggest the better surface quality [70]. The AFM height image and the corresponding line trace of the as-received wafer surface are provided in Fig. 10. As determined by the NanoScope Analysis Software (Bruker, V1.40), the average R_a , R_q , and R_z roughness over $5.0 \times 5.0 \mu\text{m}^2$ of the surface prior to polishing are 0.693, 0.829, and 1.41 nm, respectively. Meanwhile, the profile curvature tracked along the dotted line (Line 0) shows the maximum peak height (MPH) of ca. 1.83 nm and the maximum valley depth (MVP) of ca. −1.54 nm, thus revealing a peak-to-valley (PV) value of 3.37 nm. In addition, the SAD value of the pristine surface is approximately 0.093 %.

The CMP and/or PCMP performance on the three types of DMSNs, Ce–DMSNs, Ce/Cu–DMSNs abrasives were also evaluated in terms of AFM analyses. As shown in Figs. 11 and 12, the as-prepared abrasives enable the clear improvements in surface quality by comparison with the original substrate, and allow the atomically smooth and scratch-free surfaces. In addition, the surface characteristics including R_a , R_q , and R_z roughness as well as SAD data are listed in Table 1. After CMP with the Ce–DMSNs and Ce/Cu–DMSNs abrasives, the surfaces reveal a lower average R_a (0.123 and 0.141 nm), R_q (0.152 and 0.172

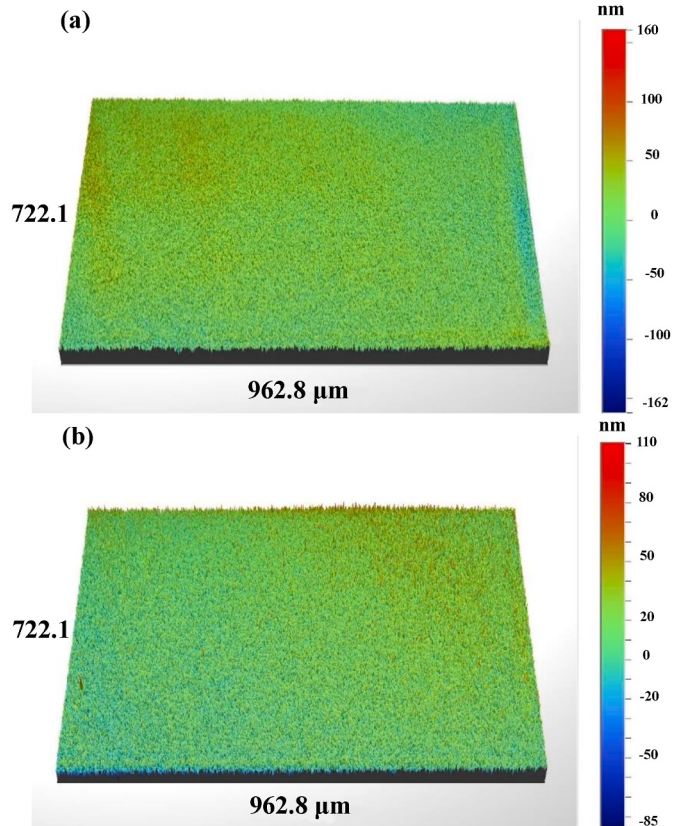


Fig. 14. Morphologies over $772.1 \times 962.8 \mu\text{m}^2$ of the surfaces after (a) CMP and (b) PCMP with Ce/Cu–DMSNs.

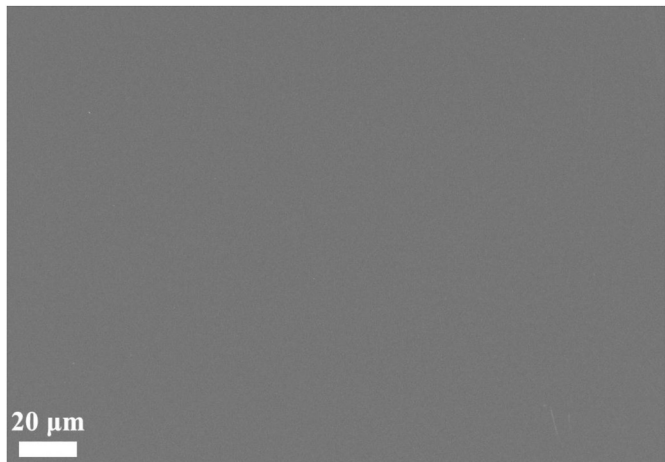


Fig. 15. SEM image of the surface after PCMP with Ce/Cu–DMSNs abrasives.

nm), and R_z (0.173 and 0.183 nm) data than those after CMP with pure DMSNs (0.167, 0.223, 0.326 nm). Moreover, the topographical variation ranges reduced from $0.50 \text{ nm} \sim -0.43 \text{ nm}$ (DMSNs, PV = 0.93 nm, Lines 1 and 2) to $0.43 \text{ nm} \sim -0.38 \text{ nm}$ (Ce–DMSNs, PV = 0.81 nm, Lines 3 and 4) and $0.35 \text{ nm} \sim -0.41 \text{ nm}$ (Ce/Cu–DMSNs, PV = 0.76 nm, Lines 5 and 6). And the average SAD data decreased from 0.00645 % (DMSNs) to 0.00355 % (Ce–DMSNs) and 0.00358 % (Ce/Cu–DMSNs). The results of AFM analyses clearly confirm that the Ce single-doping and Ce/Cu co-doping contribute to the surface quality improvement for the DMSNs–based abrasive systems. In this work, the best surface quality was achieved with Ce/Cu–DMSNs abrasive systems under PCMP

conditions. Herin, the Ce/Cu–DMSNs offered the smallest average R_a (0.120 nm), R_q (0.144 nm), and R_z (0.149 nm) roughness as well as SAD data (0.00299 %). And the corresponding MPH and MVP are 0.35 and -0.45 nm ($\text{PV} = 0.80 \text{ nm}$, Lines 7 and 8), respectively.

The morphological evolutions of the surfaces before and after CMP and/or PCMP with DMSNs-based abrasives were also tracked in terms of the 3D-AFM images and the lateral views driven from the corresponding 2D-AFM height images. As shown in Fig. 13, the Ce single-doped and Ce/Cu co-doped DMSNs abrasives effectively remove the most of nano-peaks at the original surfaces without introducing other new damages or scratches, contributing to topographical variation reductions and thus revealing superior planarization performance. In addition, the wafers after CMP and PCMP with Ce/Cu–DMSNs particles were selected for surface morphology examinations at a large scanning scale of $772.1 \times 962.8 \mu\text{m}^2$. As shown in Fig. 14, the finished workpieces present ultra-smooth mirror appearances, and obvious surface defects such as residues, scratches, pits, cracks, etc. can hardly be observed.

Generally, the CeO_2 abrasives with smaller sizes and/or more surface Ce(III) sites can strongly adhere to the SiO_2 surfaces due to the created Ce–O–Si bonds during and after polishing [71]. Herein, the results of SEM observations (Fig. 15) on the surfaces after PCMP with Ce/Cu–DMSNs abrasives verify that the adhered particles can be effectively removed from the SiO_2 surfaces without polluting the polished samples. The Ce–DMSNs and Ce/Cu–DMSNs abrasives in used PCMP slurries were also collected and detected by SEM in order to estimate the particle structure stability. With respect to the original particles (Fig. 3), there are no clear changes in particle morphology, size and distribution, as presented in Fig. 16, thus revealing the good structure stabilities of the as-synthesized abrasives under the interface contact, friction and wear involved in material removal processes.

In CMP applications, the ultimate surface quality, defect, and damage can be regarded as a consequence of the interfacial interaction between abrasives and substrates, which will be highly affected by the properties of abrasive particles in slurries, such as type, morphology, structure, component, particle size and distribution, mechanical properties (typically elastic modulus E and hardness), etc. As reported in our previous work [34], the average E values of individual DMSNs (ca. 5.0 nm of pore size) were determined to be ca. 4.5 GPa using AFM force-curve technique and Hertz contact model, which were much lower than those of nonporous SiO_2 materials (72–76 GPa [72]). In this work, the as-prepared DMSNs–based nanospheres with large porosity and abundant mesopores (ca. 9.0 nm of pore size) may also feature the reduced overall modulus and hardness, which can contribute to the optimization of physical contact behavior between the abrasive and the workpiece. The schematic illustration of the possible interface contacts between the substrate surface and the DMSNs–based abrasive is proposed in Fig. 17. During CMP and PCMP processes, the low-modulus DMSNs–involved particles might undergo slightly elastic deformation under an applied down force, thus avoiding the surface damage originated from hard abrasive collisions. It can also help reduce the indentation depth and increase the real contact area between the abrasives and the surfaces [16,21–23,28,32–36,73–75]. Consequently, the DMSNs–based abrasives offered the superior surface quality, e.g., nearly defect-free and atomic-level finish. The developed abrasive systems can better meet the requirements of advanced polishing slurry abrasives for achieving high-quality surfaces.

3.3.2. Removal efficiency

Material removal efficiency (or MRR) is another critical indicator for evaluating polishing performance. Herein, the MRR data of three abrasive types are summarized in Table 2. For CMP processes, the average MRR of Ce/Cu–DMSNs is 152 nm/min, which is a 123.5 % and 63.4 % increases with respect to those of DMSNs (68 nm/min) and Ce/Cu–DMSNs (93 nm/min), respectively. Under PCMP experimental conditions, the Ce/Cu–DMSNs abrasive systems achieved the highest average MRR of 184 nm/min. These results clearly indicate that both

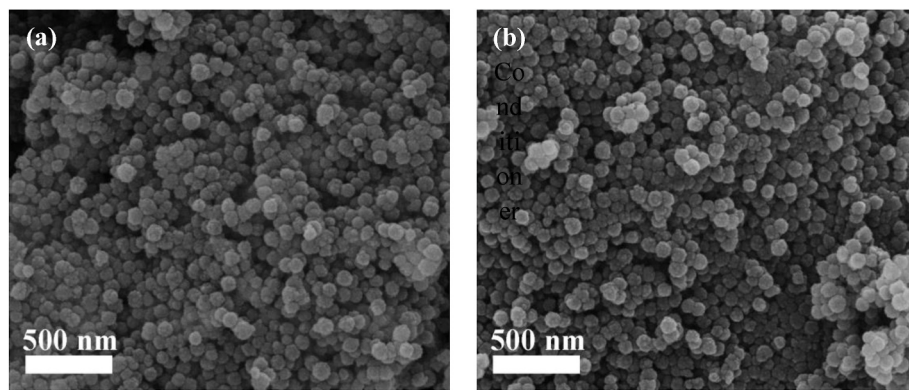


Fig. 16. SEM images of the (a) Ce–DMSNs and (b) Ce/Cu–DMSNs particles in used PCMP slurries.

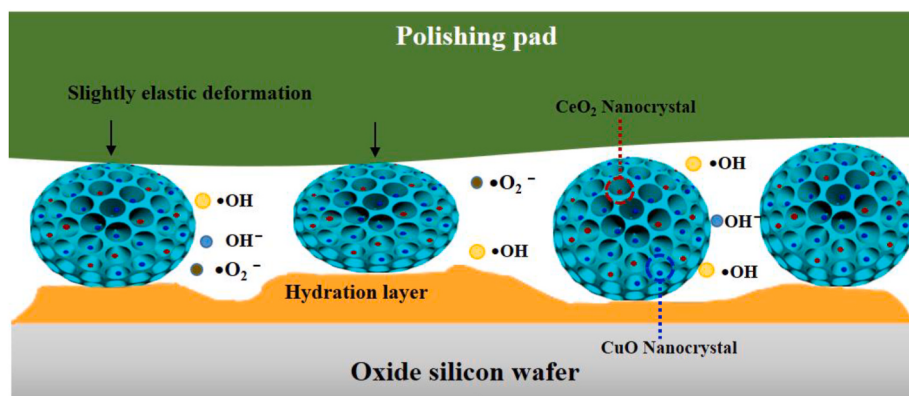


Fig. 17. The schematic illustration of the possible interface contact between the substrate and the DMSNs abrasive.

Table 2

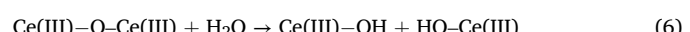
MRR data achieved with different DMSNs-involved abrasive systems.

Abrasives	MRR (nm/min)				
	Run 1	Run 2	Run 3	Average	Standard deviation
DMSNs (CMP)	62	72	70	68	5
Ce–DMSNs (CMP)	97	94	89	93	4
Ce/Cu–DMSNs (CMP)	138	156	162	152	12
Ce/Cu–DMSNs (PCMP)	190	188	174	184	9

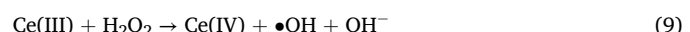
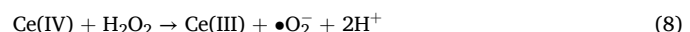
Ce/Cu co-doping treatment and UV irradiation introduction are conducive to enhancing the removal efficiency of DMSNs-based abrasives.

It is generally recognized that the *MRR* on SiO₂–CMP depends on the surface modification/corrosion and the friction/abrasion removal. The circular formation and removal of the chemically reacted productions play a crucial role in the final *MRR*. In the case of SiO₂–polishing with CeO₂ abrasives, the tribochemical process or chemical-tooth theory (the formation and breakage of Ce–O–Si bonds) was first proposed by Cook [76]. In-depth investigations [77–83] further confirm that the surface Ce (III) sites can be expected to be active sites for the formation of Ce(III)–O–Si structures. Typically, the Ce(III)–OH bonding at CeO₂ surfaces could react with Si–OH bonding at SiO₂ surfaces and thus produced Ce (III)–O–Si structures, as described in equations (6) and (7). After Ce–O–Si bond formations, the free electrons in Ce(III) might migrate to the SiO₂ surface, further weakening or even breaking the stable Si–O covalent bonds [83,84]. As a consequence, the formation and breakage of Ce(III)–O–Si bonds are responsible for the enhanced removal

efficiency of CeO₂ toward SiO₂.



For Ce–DMSNs samples, the comprehensive analyses of XRD, HRTEM, N₂ adsorption–desorption, and EDS maps suggest that there are some CeO₂ nanocrystals located at DMSNs surfaces or formed within DMSNs mesochannels. XPS results further confirm the coexistence of Ce (III) and Ce(IV) species. In this work, the constructed Ce–DMSNs materials can also be expected to be a simple heterogeneous Fenton-like system in the presence of H₂O₂. The catalytic decomposition of H₂O₂ by Ce(III)/Ce(IV) couples can generate highly active ROS such as •OH, •O₂⁻, etc., as shown in equations (8) and (9) [85]. As proposed in literatures [24,36], the produced ROS (typically •OH) may also react with the SiO₂, thus accelerating the Si–O–Si bond breakage and the Si–OH and Si(OH)₄ formations, as shown in equation (10).



As proposed by reactive molecular dynamics simulations [82], the SiO₂ surface with a higher degree of hydroxylation (thicker Si(OH)₄ layer) might be more reactive, implying that proper chemical treatment should be fundamental to augment the removal efficiency. The developed Ce–DMSNs abrasives can be expected to contribute to the formation and breakage of Si–OH and/or Ce(III)–O–Si bonds, possibly due to the tribochemical activity of CeO₂ and the generated ROS in Fenton-like reaction. Consequently, the Ce–DMSNs abrasives achieve a higher average *MRR* (93 nm/min) than that of bare DMSNs ones (68

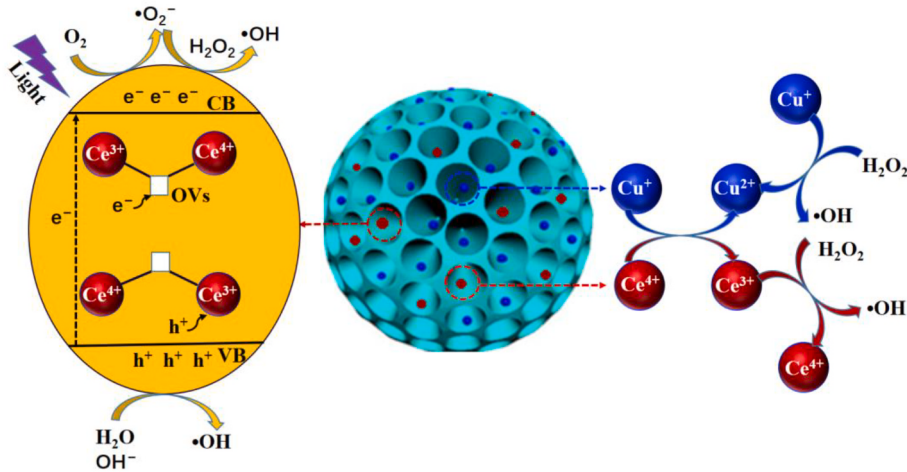


Fig. 18. The schematic illustration of the possible ROS production mechanism for Ce/Cu–DMSNs.

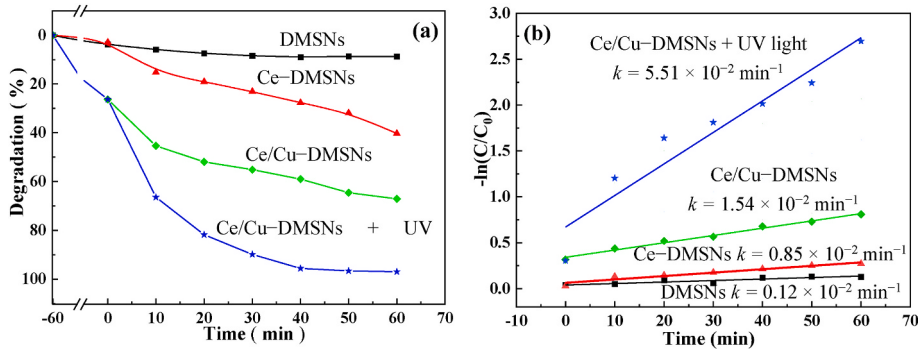
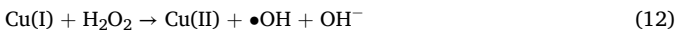
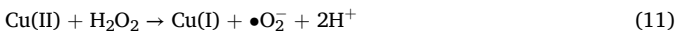


Fig. 19. Degradation efficiency curves (a) and the plot of $-\ln(C/C_0)$ versus degradation time (b) of DMSNs, Ce–DMSNs, and Ce/Cu–DMSNs samples.

nm/min).

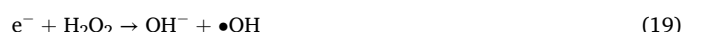
Heterogeneous Fenton-like reactions with transition metal ions (typically Cu, Co, Mn, etc.) at low oxidation states and H_2O_2 have been confirmed to be available and effective AOP processes. For Ce/Cu–DMSNs materials, more ROS (typically $\bullet\text{OH}$) can be produced after introducing the variable valence element of Cu, possibly resulting from the synergy between CuO with CeO_2 and the electron transfer between Cu(I)/Cu(II) and Ce(III)/Ce(IV) [86], as described in equation (11)–(14). It further contributes to the formation of Si–OH structure at SiO_2 surfaces. Fig. 18 shows the schematic illustration of the possible ROS production mechanism for Ce/Cu–DMSNs.



XPS results reveal that the Ce/Cu–DMSNs possess more Ce(III) ions (ca. 39.5 %) than that of Ce–DMSNs (ca. 32.8 %), further contributing to the formation and breakage of Ce(III)–O–Si bonding. The enhanced surface modification and tribocorrosion reaction can be responsible for the effective removal against SiO_2 materials. Therefore, the co-doped Ce/Cu–DMSNs abrasive systems allow an evidently enhanced CMP-MRR (152 nm/min in average) compared to the single-doped Ce–DMSNs ones (93 nm/min in average).

In the UV irradiation-assisted PCMP with Ce/Cu–DMSNs, the photocatalysis activity of CeO_2 nanocrystals may be also involved in the ROS productions. When the slurry abrasives were irradiated by UV light, the

photoexcited electrons (e^-) from the valence band (VB) of CeO_2 could be transferred to the conduction band (CB) of CeO_2 , thereby creating positive holes (h^+) in the VB of CeO_2 . The photogenerated holes left behind in VB could oxidize the surface-adsorbed OH^- and/or H_2O to generate $\bullet\text{OH}$ radicals. The photoinduced e^- could react with H_2O_2 to create $\bullet\text{OH}$ radicals. In addition, the e^- might also reduce the surface-adsorbed O_2 and then produce the $\bullet\text{O}_2^-$ radicals, which could further react to generate $\bullet\text{OH}$ radicals. The procedures on ROS productions involved in photocatalysis are described as the following equation (15)–(20) [87]. Additionally, the surface Vo and Ce(III) defects of CeO_2 nanocrystals can be expected to serve as e^- acceptors, thereby inhibiting the recombination rate of photoinduced e^- – h^+ pairs and thus benefiting the production of active free radical groups [88]. As mentioned above, the enrichment of ROS can accelerate the formation of the Si–OH bonds at SiO_2 surfaces (chemically reacted soft layer). By comparison with CMP conditions, the Ce/Cu–DMSNs abrasive systems offer another MRR improvement in PCMP experiments (184 nm/min vs 152 nm/min).



In this work, the ROS production efficiencies of the pure and doped DMSNs were also validated in terms of the degradation tests over TC.

The variation in TC concentration with degradation time and the plot of $-\ln(C/C_0)$ versus degradation time are shown in Fig. 19. The presented data reveal that degradation efficiencies follow the order: Ce/Cu–DMSNs (with UV irradiation) > Ce/Cu–DMSNs > Ce–DMSNs > DMSNs. With the assistance of UV irradiation, the Ce/Cu co-doped DMSNs greatly shorten the degradation time, and achieve the highest TC degradation efficiency of 98.1 % in 60 min with the highest degradation rate constant k of $5.51 \times 10^{-2} \text{ min}^{-1}$. These results support that the Ce/Cu–DMSNs abrasive systems are conducive to the production of more ROS in polishing slurries during UV irradiation-assisted PCMP, thus allowing superior material removal efficiency. However, the *in-situ* production of active free radicals involved in ROS-assisted polishing can hardly be monitored due to their extremely short lifetime [89,90]. In the subsequent work, more solid evidence on the generated ROS and active sites will be further investigated in terms of electron paramagnetic resonance, electron spin resonance, free radical quenching experiments, tip-enhanced Raman spectroscopy, *in-situ* FT-IR, *in-situ* Raman, etc.

4. Conclusions

In this work, the Ce single-doped and Ce/Cu co-doped DMSNs were synthesized by a simple impregnation–calcination procedure and characterized by several state-of-the-art techniques, and then applied in ROS-enhanced polishing as novel abrasive systems. SEM, TEM, and nitrogen adsorption–desorption studies revealed that there were no appreciable changes in particle size, pore diameter, and mesoporous nature. FT-IR investigations implied the existence of Ce–O–Si and/or Cu–O–Si structures in the doped DMSNs matrixes. XRD results confirmed the presence of crystalline CeO₂ and CuO, which might be exposed on the surfaces and located within the mesopores of the doped DMSNs. XPS and EDS analyses further supported the coexistence of Ce (III)/Ce(IV) and Cu(I)/Cu(II) couples in Ce/Cu–DMSNs materials. The results of polishing tests towards SiO₂ indicated that three type of DMSNs-involved abrasives enabled high-quality and defect-free surfaces with atomic-level finish (0.12–0.14 nm of Ra, 0.14–0.18 nm of Rq). The low-modulus DMSNs carriers might be responsible for optimizing abrasive–surface interfacial contact and thus achieving soft polishing or soft abrasion. Upon UV irradiation-assisted PCMP, the synergy of Cu(I)/Cu(II) and Ce(III)/Ce(IV) couples was conducive to the ROS productions in photocatalysis and Fenton-like reactions, thus accelerating the formation of the chemically reacted layer (Si–OH structures). Furthermore, the incorporation of Ce(III) species contributed to promoting the material removal through the solid-state tribochemical reaction (the generation of Ce–O–Si bonds). As a consequence, the material removal efficiencies followed the order of Ce/Cu–DMSNs (PCMP, 184 nm/min) > Ce/Cu–DMSNs (CMP, 152 nm/min) > Ce–DMSNs (CMP, 93 nm/min) > DMSNs (CMP, 68 nm/min). The nano-scale impregnation of metal ions onto mesoporous silica has many advantages such as high elasticity and high chemical or photochemical and tribochemical activity for the development of novel abrasive systems. The presented methodology is highly promising for the synthesis of many other metal-doped meso-SiO₂ materials that can find numerous applications in various fields.

CRediT authorship contribution statement

Wenjin Zhou: Writing – original draft, Methodology, Investigation. **Yang Chen:** Writing – review & editing, Validation, Formal analysis, Conceptualization. **Chao Wang:** Supervision, Project administration, Methodology, Funding acquisition. **Menghan Wang:** Visualization, Software, Investigation, Data curation. **Ailian Chen:** Supervision, Resources, Project administration, Funding acquisition.

Declaration of competing interest

The authors declare that they have no known competing financial

interests or personal relationships that could have appeared to influence the work reported in this paper.

Acknowledgements

The work was supported by the National Natural Science Foundation of China (Grant Nos. 52275174, 52175444, and 51875052), and the Sichuan Science and Technology Program (2021JDJQ0014).

References

- [1] X. Wang, Y. Dai, Y. Li, L. Yin, Application of advanced oxidation processes for the removal of micro/nanoplastics from water: a review, *Chemosphere* 346 (2024) 140636.
- [2] J. Tan, X. Zhang, Y. Lu, X. Li, Y. Huang, Role of interface of metal–organic frameworks and their composites in persulfate-based advanced oxidation process for water purification, *Langmuir* 40 (2024) 21–38.
- [3] Y. Gao, P. Wang, Y. Chu, F. Kang, Y. Cheng, E. Repo, M. Feng, X. Yu, H. Zeng, Redox property of coordinated iron ion enables activation of O₂ via *in-situ* generated H₂O₂ and additionally added H₂O₂ in EDTA-chelated Fenton reaction, *Water Res.* 248 (2024) 120826.
- [4] P.M. Septilveda, S.A. Campos, W. Calzadilla, J.F. Marco, J.C. Denardin, R. A. Salazar-González, Pd-based nanoparticles as catalysts for improved removal of florenicol via heterogeneous Fenton and photo-Fenton(-like) processes, *ACS Appl. Nano Mater.* 6 (2023) 12177–12189.
- [5] R. Li, Y. Li, X. Jia, J. Yang, X. Miao, D. Shao, J. Wu, H. Song, 2D/2D ultrathin polypyrole heterojunct aerogel with synergistic photocatalytic-photothermal evaporation performance for efficient water purification, *Desalination* 574 (2024) 117295.
- [6] H. Wen, W. Zhang, Z. Fan, Z. Chen, Recent advances in furfural reduction *via* electro- and photocatalysis: from mechanism to catalyst design, *ACS Catal.* 13 (2023) 15263–15289.
- [7] J. Deng, J. Pan, Q. Zhang, Q. Yan, J. Lu, The mechanism of Fenton reaction of hydrogen peroxide with single crystal 6H-SiC substrate, *Surface. Interfac.* 21 (2020) 100730.
- [8] X. Wang, Q. Xiong, J. Lu, Q. Yan, W. Liu, Characterization of Fenton reaction-based material removal on single crystal diamond surface, *Diam. Relat. Mater.* 129 (2022) 109320.
- [9] S. Yuan, X. Guo, M. Li, Z. Jin, D. Duo, An insight into polishing slurry for high quality and efficiency polishing of diamond, *Tribol. Int.* 174 (2022) 107789.
- [10] X. Wang, Q. Xiong, J. Lu, Q. Yan, W. Liu, Characterization of Fenton reaction-based material removal on single crystal diamond surface, *Diam. Relat. Mater.* 129 (2022) 109320.
- [11] J. Pan, Z. Zhuo, Q. Zhang, Q. Zheng, Q. Yan, Friction and wear mechanisms for single crystal GaN based on an electro-Fenton enhanced chemical reaction, *Wear* 498 (2022) 204315.
- [12] J. Pan, Y. Wu, Z. Zhuo, H. Wang, Q. Zheng, Q. Yan, Experimental study of single-crystal GaN wafer electro-Fenton magnetorheological complex friction wear, *Tribol. Int.* 180 (2023) 108260.
- [13] W. Cai, J. Lu, Q. Xiong, Z. Luo, Q. Yan, Tribological behavior of polycrystalline diamond based on photo-Fenton reaction, *Diam. Relat. Mater.* 140 (2023) 110430.
- [14] D. Hu, J. Lu, J. Deng, Q. Yan, H. Long, Y. Luo, The polishing properties of magnetorheological-elastomer polishing pad based on the heterogeneous Fenton reaction of single-crystal SiC, *Precis. Eng.* 79 (2023) 78–85.
- [15] J. Pan, Y. Wu, Z. Zhuo, H. Wang, Q. Zheng, Q. Yan, Experimental study of single-crystal GaN wafer electro-Fenton magnetorheological complex friction wear, *Tribol. Int.* 180 (2023) 108260.
- [16] Y. Chen, A. Wei, X. Ma, T. Wang, A. Chen, Copper-incorporated dendritic mesoporous silica nanospheres and enhanced chemical mechanical polishing (CMP) performance *via* Cu²⁺/H₂O₂ heterogeneous Fenton-like system, *Appl. Surf. Sci.* 601 (2022) 154262.
- [17] K. Kim, K. Lee, S. So, S. Cho, M. Lee, K. You, J. Moon, T. Song, Fenton-Like reaction between copper ions and hydrogen peroxide for high removal rate of tungsten in chemical mechanical planarization, *ECS. J. Solid. State. Sci. Technol.* 7 (2018) P91–P95.
- [18] S. Chen, H. Lei, Polishing performance and mechanism of a novel Fe-based slurry for chemical mechanical polishing, *Tribol. Int.* 194 (2024) 109549.
- [19] Q. Yan, X. Wang, Q. Xiong, J. Lu, B. Liao, The influences of technological parameters on the ultraviolet photocatalytic reaction rate and photocatalysis-assisted polishing effect for SiC, *J. Cryst. Growth* 531 (2020) 125379.
- [20] N. Xu, Y. Luo, J. Ma, Y. Lin, X. Zhu, Y. Pu, Enhancement mechanism of Y-doped Ce_{1-x}Y_xO₂ for photocatalytic-assisted chemical-mechanical polishing, *Mater. Today Commun.* 38 (2024) 107791.
- [21] Y. Chen, L. Zhong, A. Chen, M. Fu, X. Lu, Highly dispersed Gd-CeO₂ nanocrystals supported on mesoporous silica composite particles towards photochemical (photo-assisted chemical) mechanical polishing, *Ceram. Int.* 49 (2023) 16932–16943.
- [22] A. Chen, T. Wang, Y. Chen, S. Wang, Y. Chen, Development of polystyrene/polyaniline/ceria (PS/PANI/CeO₂) multi-component abrasives for photochemical mechanical polishing/planarization applications, *Appl. Surf. Sci.* 575 (2022) 151784.
- [23] B. Gao, W. Zhai, Q. Zhai, M. Zhang, Novel polystyrene/CeO₂-TiO₂ multicomponent core/shell abrasives for high-efficiency and high-quality photocatalytic-assisted

- chemical mechanical polishing of reaction-bonded silicon carbide, *Appl. Surf. Sci.* 484 (2019) 534–541.
- [24] Y. Fan, Z. Zhang, J. Yu, X. Deng, C. Shi, H. Zhou, F. Meng, J. Feng, Atomic surface of quartz glass induced by photocatalytic green chemical mechanical polishing using the developed $\text{SiO}_2@\text{TiO}_2$ core–shell slurry, *Nanoscale Adv.* 6 (2024) 1380–1391.
- [25] X. Zhu, Y. Gui, H. Fu, J. Ding, Z. Mo, X. Jiang, J. Sun, B. Ban, L. Wang, J. Chen, Photocatalytic assisted chemical mechanical polishing for silicon carbide using developed ceria coated diamond core–shell abrasives, *Tribol. Int.* (2024), <https://doi.org/10.1016/j.triboint.2024.109827>.
- [26] W. Jiang, H. Zhou, Y. Yang, S. Hu, J. Song, J. Ji, J. Song, A synergistic polishing technology by mixed abrasives with photocatalysis and Fenton reaction, *Mater. Sci. Semicond. Process.* 166 (2023) 107734.
- [27] J. Lu, Y. Huang, Y. Fu, Q. Yan, S. Zeng, Synergistic effect of photocatalysis and Fenton on improving the removal rate of 4H-SiC during CMP, *ECS. J. Solid. State. Sci. Technol.* 10 (2021) 044001.
- [28] B. Gao, W. Zhai, Q. Zhai, C. Wang, Novel photoelectrochemically combined mechanical polishing technology for scratch-free 4H-SiC surface by using $\text{CeO}_2\text{-TiO}_2$ composite photocatalysts and PS/ CeO_2 core/shell abrasives, *Appl. Surf. Sci.* 570 (2021) 151141.
- [29] R. Ding, H. Lei, L. Xu, Y. Chen, Surface planarization of zirconia ceramic achieved by polyacrylamide grafted nanodiamond composite abrasives through chemical mechanical polishing, *Ceram. Int.* 48 (2022) 19900–19912.
- [30] N. Xu, Y. Luo, Y. Lin, J. Ma, Y. Pu, The influence of CeO_2 abrasive size on the performance of photocatalytic assisted chemical-mechanical polishing by Y/Pr co-doping strategy, *Colloids Surf., A* 684 (2024) 133107.
- [31] E. Kim, J. Lee, C. Bae, H. Seok, H. Kim, T. Kim, Effects of trivalent lanthanide (La and Nd) doped ceria abrasives on chemical mechanical polishing, *Powder Technol.* 397 (2022) 117025.
- [32] Y. Fan, J. Jiao, L. Zhao, J. Tang, Preparation of lanthanide-doped polystyrene/ CeO_2 abrasives and investigation of slurry stability and photochemical mechanical polishing performance, *Colloid. Surface.* 656 (2023) 130508.
- [33] A. Chen, S. Wang, J. Pan, T. Wang, Y. Chen, Development of Zr- and Gd-doped porous ceria (pCeO_2) abrasives for achieving high-quality and high-efficiency oxide chemical mechanical polishing, *Ceram. Int.* 48 (2022) 14039–14049.
- [34] A. Chen, S. Wang, W. Cai, Z. Mu, Y. Chen, Tunable synthesis, characterization, and CMP performance of dendritic mesoporous silica nanospheres as functionalized abrasives, *Colloid. Surface.* 638 (2022) 128322.
- [35] Y. Fan, J. Jiao, L. Zhao, J. Tang, C. Chen, N. Fan, Nd-doped porous CeO_2 abrasives for chemical mechanical polishing of SiO_2 films, *Mater. Sci. Semicond. Process.* 175 (2024) 108265.
- [36] M. Wang, Z. Mu, T. Wang, Y. Chen, A. Chen, Double-layered core–shell heterostructures of $\text{mSiO}_2@\text{CdS}@\text{CeO}_2$ abrasive systems toward photochemical mechanical polishing (PCMP) applications, *Appl. Surf. Sci.* 614 (2023) 156274.
- [37] C. Shi, Y. Fan, Z. Zhang, X. Deng, J. Yu, H. Zhou, F. Meng, J. Feng, Development of core–shell $\text{SiO}_2@\text{A-TiO}_2$ abrasives and novel photocatalytic chemical machinal polishing for atomic surface of fused silica, *Appl. Surf. Sci.* 652 (2024) 159293.
- [38] L. Wang, G. Ren, W. Xie, J. Zhang, D. Pan, H. Su, S. Wang, Controllable synthesis of core-shell $\text{SiO}_2@\text{CeO}_2$ abrasives for chemical mechanical polishing on SiO_2 film, *Colloid. Surface.* 682 (2024) 132901.
- [39] C. Chen, Y. Cui, X. Li, S. Shen, W. Liao, H. You, Novel ceria/graphene oxide composite abrasives for chemical mechanical polishing, *Ceram. Int.* (2024), <https://doi.org/10.1016/j.ceramint.2024.03.193>.
- [40] P. Gao, T. Liu, Z. Zhang, F. Meng, R. Ye, J. Liu, Non-spherical abrasives with ordered mesoporous structures for chemical mechanical polishing, *Sci. China Mater.* 64 (2021) 2747–2763.
- [41] L. Xu, H. Lei, Z. Ding, Y. Chen, R. Ding, T. Kim, Preparation of the rod-shaped $\text{SiO}_2@\text{C}$ abrasive and effects of its microstructure on the polishing of zirconia ceramics, *Powder Technol.* 395 (2022) 338–347.
- [42] L. Bian, W. Deng, D. Xie, X. Sun, Y. Huo, Y. Zhang, F. Chen, J. Hu, Dendritic mesoporous silica hollow spheres with one-pot self-templated interfacial diffusion method, *Chem. Mater.* 36 (2024) 482–491.
- [43] X. Yang, K. Quan, J. Wang, J. Liu, B. Liu, J. Chen, M. Guan, H. Qiu, Particle size and pore adjustment of dendritic mesoporous silica using different long alkyl-chain imidazolium ionic liquids as templates, *Microporous Mesoporous Mater.* 345 (2022) 112249.
- [44] T. Liu, H. Lei, Nd³⁺-doped colloidal SiO_2 composite abrasives: synthesis and the effects on chemical mechanical polishing (CMP) performances of sapphire wafers, *Appl. Surf. Sci.* 413 (2017) 16–26.
- [45] H. Lei, T. Liu, L. Xu, Synthesis of Sm-doped colloidal SiO_2 composite abrasives and their chemical mechanical polishing performances on sapphire substrates, *Mater. Chem. Phys.* 237 (2019) 121819.
- [46] D. Shen, J. Yang, X. Li, L. Zhou, R. Zhang, W. Li, L. Chen, R. Wang, F. Zhang, D. Zhao, Biphase stratification approach to three-dimensional dendritic biodegradable mesoporous silica nanospheres, *Nano Lett.* 14 (2014) 923–932.
- [47] Y. Li, J. Ying, T. He, G. Li, H. Zhang, S. Huang, T. Huang, W. Liu, H. Peng, Ultra-small Pt–Ni bimetallic nanoparticles confined in dendritic mesoporous silica with remarkable CO catalytic oxidation performance, *Ind. Eng. Chem. Res.* 62 (2023) 9159–9168.
- [48] F. Hachebe, B. Boukoussa, I. Issam, A. Mokhtar, X. Lu, J. Iqbal, F. Benali, S. Hacini, M. Hachemoui, M. Abboud, Synthesis and application of metal nanoparticles-loaded mesoporous silica toward the reduction of organic pollutants in a simple and binary system, *Inorg. Chem. Commun.* 151 (2023) 110572.
- [49] L. Hao, Z. Jiang, Y. Fang, Y. Zhou, B. Fu, L. Lin, Understanding the role of oxygen vacancy on corrosion resistance of coating containing cerium oxide nanoparticles doped with cobalt as highly effective corrosion inhibitors, *Appl. Surf. Sci.* 626 (2023) 157300.
- [50] R. Amoresi, R. Oliveira, L. Jr, P. Desimone, C. Aldao, M. Ponce, L. Gracia, J. Sambrano, E. Longo, J. Andres, A. Simoes, Pure and Ni_2O_3 -decorated CeO_2 nanoparticles applied as CO gas sensor: experimental and theoretical insights, *Ceram. Int.* 48 (2022) 14014–14025.
- [51] T. Tsioncheva, G. Issaa, T. Blascob, M. Dimitrova, M. Popovaa, S. Hernándezb, D. Kovachevac, G. Atanasovac, L. Nieto, Catalytic VOCs elimination over copper and cerium oxide modified mesoporous SBA-15 silica, *Appl. Catal. A* 453 (2013) 1–12.
- [52] M.A. Mavuso, P.R. Makgware, S.S. Ray, Heterostructured $\text{CeO}_2\text{-M}$ (M = Co, Cu, Mn, Fe, Ni) oxide nanocatalysts for the visible-light photooxidation of pinene to aroma oxygenates, *ACS Omega* 5 (2020) 9775–9788.
- [53] S. Xu, J. Wu, Z. Ren, D. Niu, Precise phase adjustment and antibacterial property of copper sulfide particles in confined mesoporous silica nanoreactor, *Particuology* 85 (2024) 113–121.
- [54] B. Yang, W. Deng, L. Guo, T. Ishihara, Copper-ceria solid solution with improved catalytic activity for hydrogenation of CO_2 to CH_3OH , *Chinese J. Catal.* 41 (2020) 1348–1359.
- [55] D. Wu, J. Zhang, Z. Huang, J. Chen, Cerium-modified copper/hexagonal mesoporous silica catalyst for efficient dimethyl oxalate hydrogenation to ethylene glycol under moderate reaction conditions, *J. Fuel Chem. Technol.* 51 (2023) 186–196.
- [56] M. Yadav, M. Dhanda, R. Arora, S. Ahlawat, G. Singh, K. Nehra, S. Lata, Dual applicability of ceria and silica nanospheres ($\text{CeO}_2@\text{SiO}_2$ NSS) assembled with pencil graphite electrode to sense ascorbic acid, extended with their antibacterial property, *Mater. Sci. Eng., B* 297 (2023) 116719.
- [57] M. Jang, J.K. Park, E.W. Shin, Lanthanum functionalized highly ordered mesoporous media: implications of arsenate removal, *Microporous Mesoporous Mater.* 75 (2004) 159–168.
- [58] K. Parida, D. Rath, Surface characterization and catalytic evaluation of copper-promoted Al-MCM-41 toward hydroxylation of phenol, *J. Colloid Interface Sci.* 340 (2009) 209–217.
- [59] L. Wang, A. Kong, B. Chen, H. Ding, Y. Shan, M. He, Direct synthesis, characterization of Cu-SBA-15 and its high catalytic activity in hydroxylation of phenol by H_2O_2 , *J. Mol. Catal. A* 230 (2005) 143–150.
- [60] Y. Wang, H. Ma, J. Guo, Y. Han, X. Ding, Y. Zhang, TiO_{2-x} nanoparticles dispersed in center-radial channels of dendritic mesoporous silica nanospheres (DMSNs) as novelly structured photocatalysts, *J. Mater. Sci.* 56 (2021) 14659–14671.
- [61] J. Ding, C. Xu, G. Fan, T. Naren, Y. Wang, Y. Liu, X. Gu, L. Wu, S. Zeng, Engineering CeO_2 configurations to regulate the CuO_x dispersion and switch pathways of preferential CO oxidation, *Appl. Catal., B* 331 (2023) 122686.
- [62] S. Chen, L. Li, W. Hu, X. Huang, Q. Li, Y. Xu, Y. Zuo, G. Li, Anchoring high-concentration oxygen vacancies at interfaces of $\text{CeO}_{2-x}/\text{Cu}$ toward enhanced activity for preferential CO oxidation, *ACS Appl. Mater. Interfaces* 7 (2015) 22999–23007.
- [63] Y. Xing, J. Wu, C. Zhang, L. Zhang, J. Han, D. Liu, H. Wang, X. Hou, Z. Gao, Mn-induced Cu/Ce catalysts with improved performance for CO preferential oxidation in H_2/CO_2 -rich streams, *Int. J. Hydrogen Energy* 48 (2023) 20667–20679.
- [64] H. Zhang, X. Zhao, S. Wang, S. Zeng, H. Su, Change of Cu^{+} species and synergistic effect of copper and cerium during reduction-oxidation treatment for preferential CO oxidation, *Appl. Surf. Sci.* 441 (2018) 754–763.
- [65] Y. Zheng, K. Li, H. Wang, Y. Wang, D. Tian, Y. Wei, X. Zhu, C. Zeng, Y. Luo, Structure dependence and reaction mechanism of CO oxidation: a model study on macroporous CeO_2 and $\text{CeO}_2\text{-ZrO}_2$ catalysts, *J. Catal.* 344 (2016) 365–377.
- [66] Y. He, J. Liu, G. Zhang, Y. Wang, Y. Zhao, G. Li, Y. Zhang, D. Lv, Interfacial effects promote the catalytic performance of $\text{CuCoO}_2\text{-CeO}_2$ metal oxides for the selective reduction of NO by CO, *Chem. Eng. J.* 465 (2023) 142856.
- [67] X. Li, S. Ren, Z. Chen, L. Chen, M. Wang, L. Wang, A. Wang, Promoting mechanism of CuO on catalytic performance of CeFe catalyst for simultaneous removal of NO_x and CO, *Fuel* 347 (2023) 128435.
- [68] F. Akgul, G. Akgul, N. Yildirim, H. Unalan, R. Turan, Influence of thermal annealing on microstructural, morphological, optical properties and surface electronic structure of copper oxide thin films, *Mater. Chem. Phys.* 147 (2014) 987–995.
- [69] S. Dolai, R. Dey, S. Das, S. Hussain, R. Bhar, A. Pal, Cupric oxide (CuO) thin films prepared by reactive d.c. magnetron sputtering technique for photovoltaic application, *J. Alloys Compd.* 724 (2017) 456–464.
- [70] J. Ma, N. Xu, J. Hu, Y. Luo, Y. Lin, Y. Pu, Doping strategy on properties and chemical mechanical polishing performance of CeO_2 Abrasives: a DFT assisted experimental study, *Appl. Surf. Sci.* 623 (2023) 156997.
- [71] C.K. Ranaweera, S.V. Babu, S. Hamada, J. Seo, Measurement of the force required to move ceria particles from SiO_2 surfaces using lateral force microscopy, *J. Mater. Res.* 37 (2022) 1789–1797.
- [72] S. Romeis, J. Paul, P. Herre, D. de Ligny, J. Schmidt, W. Peukert, Local densification of a single micron sized silica sphere by uniaxial compression, *Scripta Mater.* 108 (2015) 84–87.
- [73] X. Yuan, C. Chen, H. Lei, Z. Zhang, Synthesis, characterization of $\text{CeO}_2@ZIF-8$ composite abrasives and their chemical mechanical polishing behavior on glass substrate, *Ceram. Int.* 49 (2023) 5189–5198.
- [74] J. Ryu, W. Kim, J. Yun, K. Lee, J. Lee, H. Yu, J. Kim, J. Kim, J. Jang, Fabrication of uniform wrinkled silica nanoparticles and their application to abrasives in chemical mechanical planarization, *ACS Appl. Mater. Interfaces* 10 (2018) 11843–11851.

- [75] R. Chen, R. Jiang, H. Lei, M. Liang, Material removal mechanism during porous silica cluster impact on crystal silicon substrate studied by molecular dynamics simulation, *Appl. Surf. Sci.* 264 (2013) 148–156.
- [76] L. Cook, Chemical processes in glass polishing, *J. Non-Cryst. Solids* 120 (1990) 152–171.
- [77] P.R.D. Veera, S. Peddeeti, S.V. Babu, Selective chemical mechanical polishing of silicon dioxide over silicon nitride for shallow trench isolation using ceria slurries, *J. Electrochem. Soc.* 156 (2009) H936–H943.
- [78] P.R.V. Dandu, B.C. Peethala, S.V. Babu, Role of different additives on silicon dioxide film removal rate during chemical mechanical polishing using ceria-based dispersions, *J. Electrochem. Soc.* 157 (2010) H869–H874.
- [79] R. Srinivasan, P.V.R. Dandu, S.V. Babu, Shallow trench isolation chemical mechanical planarization: a Review, *ECS J. Solid State Sci. Technol.* 4 (2015) P5029–P5039.
- [80] C.M. Netzband, K. Dunn, Investigation into the effect of CMP slurry chemicals on ceria abrasive oxidation state using XPS, *ECS J. Solid State Sci. Technol.* 8 (2019) P629–P633.
- [81] C.M. Netzband, K. Dunn, Controlling the cerium oxidation state during silicon oxide CMP to improve material removal rate and roughness, *ECS J. Solid State Sci. Technol.* 9 (2020) 044001.
- [82] L. Brugnoli, K. Miyatani, M. Akaji, S. Urata, A. Pedone, New atomistic insights on the chemical mechanical polishing of silica glass with ceria nanoparticles, *Langmuir* 39 (2023) 5527–5541.
- [83] J. Ma, N. Xu, Y. Luo, Y. Lin, Y. Pu, Enhancing the polishing efficiency of CeO₂ abrasives on the SiO₂ substrates by improving the Ce³⁺ concentration on their surface, *ACS Appl. Electron. Mater.* 5 (2023) 526–536.
- [84] T. Onodera, H. Takahashi, S. Nomura, First-principles molecular dynamics investigation of ceria/silica sliding interface toward functional materials design for chemical mechanical polishing process, *Appl. Surf. Sci.* 530 (2020) 147259.
- [85] J. Hu, B. Wu, L. Chen, C. Song, H. Yang, F. Long, J. Sun, R. Chi, Influences of CeO₂ morphology on enhanced performance of electro-Fenton for wastewater treatment, *J. Rare Earths* 40 (2022) 1870–1877.
- [86] M. Konsolakis, The role of copper–ceria interactions in catalysis science: recent theoretical and experimental advances, *Appl. Catal., B* 198 (2016) 49–66.
- [87] I. Habib, J. Burhan, F. Jaladi, C. Lim, A. Usman, N. Kumara, S. Tsang, A. Mahadi, Effect of Cr doping in CeO₂ nanostructures on photocatalysis and H₂O₂ assisted methylene blue dye degradation, *Catal. Today* 375 (2021) 506–513.
- [88] R. Xiao, Y. Zhang, S. Wang, H. Zhu, H. Song, G. Chen, H. Lin, J. Zhang, J. Xiong, Prussian blue modified CeO₂ as a heterogeneous photo-Fenton-like catalyst for degradation of norfloxacin in water, *Environ. Sci. Pollut. Res.* 28 (2021) 69301–69313.
- [89] Y. Zhou, X. Yang, C. Gong, F. Zhu, J. Wang, Y. Qi, K. Huang, J. Wu, R. Chen, Y. Liu, Recent progress in γ-Fe₂O₃-based catalysts: an overview of the synthesis and applications in environmental remediation, *Chem. Eng. J.* 475 (2023) 146198.
- [90] M. Gao, K. Wang, I. Tudela, X. Fan, Improve photocatalytic performance of g-C₃N₄ through balancing the interstitial and substitutional chlorine doping, *Appl. Surf. Sci.* 536 (2021) 147784.